Xin Zhou
Department of Mechanical Engineering,
University of Michigan,
G029 Walter E. Lay Automotive Laboratory,
1231 Beal Avenue,
Ann Arbor, MI 48109
e-mail: zhouxin@umich.edu

Dennis S. Bernstein
Professor
Department of Aerospace Engineering,
University of Michigan,
3020 FXB Building,
1320 Beal Avenue,
Ann Arbor, MI 48109
e-mail: dsbaero@umich.edu

Jeffrey L. Stein
Professor
Mem. ASME
Department of Mechanical Engineering,
University of Michigan,
2480 GG Brown Laboratories,
2350 Hayward Street,
Ann Arbor, MI 48109
e-mail: stein@umich.edu

Tulga Ersal[1]
Mem. ASME
Department or Mechanical Engineering,
University of Michigan,
G029 Walter E. Lay Automotive Laboratory,
1231 Beal Avenue,
Ann Arbor, MI 48109
e-mail: tersal@umich.edu

Battery State of Health Monitoring by Estimation of Side Reaction Current Density Via Retrospective-Cost Subsystem Identification

This paper introduces a new method to monitor battery state of health (SOH). In particular, the side reaction current density is estimated as a direct SOH indicator for the first time and its estimation is formulated as an inaccessible subsystem identification problem, where the battery health subsystem is treated as an inaccessible subsystem with the side reaction current density as the output. Inaccessibility in this context refers to the fact that the inputs and outputs of the subsystem are not measurable in situ. This subsystem is identified using retrospective-cost subsystem identification (RCSI) algorithm, and the output of the identified battery health subsystem provides an estimate for the side reaction current density. Using an example parameter set for a $LiFePO_4$ battery, simulations are performed to obtain estimates under various current profiles. These simulations show promising results in identifying the battery health subsystem and estimating the side reaction current density with RCSI under ideal conditions. Robustness of the algorithm under nonideal conditions is analyzed. Estimation of the side reaction current density using RCSI is shown to be sensitive to nonideal conditions that cause errors in the measurement or estimation of the battery voltage. A method for quantitatively assessing the impact of nonideal conditions on the side reaction current estimation accuracy is provided. The proposed estimation technique, including the method for estimating the side reaction current density using RCSI and the framework analyzing its robustness, can also be applied to other parameter sets and other battery chemistries to monitor the SOH change resulting from any electrochemical-based degradation mechanism that consumes cyclable Li-ions. [DOI: 10.1115/1.4036030]

1 Introduction

State of health (SOH) monitoring provides critical information to battery management for balancing the tradeoff between maximizing system performance and minimizing battery degradation. However, the SOH is an abstract concept that needs to be deduced from other quantities that are correlated with battery health. This paper refers to these quantities as SOH indicators.

Based on the choice of the SOH indicator, the SOH monitoring literature can be divided into two categories. Most of the literature uses battery degradation effects, such as capacity fade [1–8] and power fade [9,10], as the SOH indicator. Empirical models, such as equivalent circuit models, are often sufficient for these applications as the mapping between the SOH indicator and the battery voltage, current, and temperature. The simplicity of these models is the key advantage to these techniques. However, degradation effects can be inaccurate in representing the SOH because they are not only related to the battery SOH but are also affected by environmental conditions and use patterns [11].

The second category uses health-relevant electrochemical variables as the SOH indicator. The benefit of using these variables is that they can uniquely indicate the level of degradation independent of environmental conditions and use patterns. Some example electrochemical variables used as SOH indicators are the number of cyclable Li-ions [12,13], the solid-electrolyte-interphase (SEI) film resistance [14–19], and lithium deposition [20].

In this paper, an alternative electrochemical variable, namely the side reaction current density, is introduced as the SOH indicator. The side reaction current density is a measure of the rate of cyclable Li-ion consumption, which contributes to capacity fade in all electrochemical-based degradation mechanisms that consume cyclable Li-ions [21]. Moreover, these electrochemical mechanisms are identified to be the primary degradation mechanisms for the $LiFePO_4$ battery, which is the battery chemistry that is investigated in this research [22–24].

Although the side reaction current density is known to be associated with the degradation process [21,23], it has not been used to directly indicate the battery health in battery management applications. This paper argues that the side reaction current density is a logical choice as a direct SOH indicator in various situations because the side reaction current density provides information regarding both the degradation rate and the overall degradation level. In situations where the instantaneous degradation rate is concerned, for example where controllers are designed with avoiding dramatic degradation rate as an objective or constraint [25], the side reaction current density provides the direct measure of the degradation rate. In situations where the overall degradation level over time is concerned, such as the estimation of remaining mileages of electric vehicle batteries, the integral of the side reaction current density across the whole battery and over time provides the total loss in cyclable Li-ions, which is an electrochemical measure of the capacity loss. For degradation mechanisms that result in byproducts such as SEI film, the aforementioned integral is also proportional to the growth in internal resistance. Therefore,

[1]Corresponding author.

Contributed by the Dynamic Systems Division of ASME for publication in the Journal of Dynamic Systems, Measurement, and Control. Manuscript received March 30, 2016; final manuscript received January 8, 2017; published online June 5, 2017. Assoc. Editor: Beshah Ayalew.

this paper proposes the idea of using the side reaction current density as a direct indicator of the SOH, and provides a method to estimate the side reaction current density directly.

Compared to the other electrochemical SOH indicators [12,14,15], the side reaction current density has two advantages. First, the side reaction current density measures the rate of Li-ion consumption, thus giving an instantaneous sense of how fast a battery is degrading at each instant in time. Second, as opposed to the SEI film resistance and Lithium deposition, which are mechanism-specific indicators that apply only to the degradation mechanism of SEI film formation and Lithium plating, respectively, the side reaction current density can be applied to all Li-ion-consuming degradation mechanisms [21].

A major challenge of estimating the electrochemical SOH indicators is that they are available only from invasive or destructive methods. This paper addresses this challenge by treating the battery health system as an inaccessible subsystem of the overall battery system, and using retrospective-cost subsystem identification (RCSI) to identify this subsystem and estimate its output, namely, the side reaction current density.

This paper focuses on the following research questions:

(1) Can the side reactions that consume cyclable Li-ions and thus degrade battery health be formulated as an inaccessible subsystem in the battery?
(2) Is it possible to estimate the side reaction current density as the output of the inaccessible subsystem using RCSI?
(3) How robust is this estimation against various nonideal conditions?

This paper builds on the work in Ref. [26] with the following additional novelties. Instead of using the single particle model (SPM) [27–29] to represent the battery state of charge (SOC) system as in Ref. [26], a more detailed and accurate model, the Doyle–Fuller–Newman (DFN) model, is used in this paper. Moreover, unlike in Ref. [26] where estimation is considered only under ideal conditions, robustness of the estimation algorithm under a selection of nonideal conditions is discussed in detail in this paper to give an expectation for the performance of the algorithm in practice. These nonideal conditions include measurement noise, SOC estimation errors, modeling errors in the main system model, and form discrepancies between the subsystem and subsystem model.

The rest of the paper is organized as follows: Section 2 presents the battery model used in this paper. Section 3 discusses RCSI and its application to the estimation of the SOH. Simulation results and discussion of estimation under ideal conditions are given in Sec. 4. Section 5 provides the simulation results and discussions about robustness of the algorithm against nonideal conditions. Summary and conclusions are given in Sec. 6.

2 Battery Model

A battery model is necessary in this study for two reasons. First, the inaccessible subsystem estimation algorithm RCSI requires a map relating the inaccessible quantity to the signals that are measurable in practice. In this work, this map is a battery model that relates the side reaction current density to the battery terminal voltage and current. Second, because the investigation in this paper is simulation based, a battery model is required to represent a battery.

This section presents the battery model used in this work. An electrochemical model is adopted to support the use of an electrochemical SOH indicator. Two forms of this model are given. The first form, the electrochemical form, includes the electrochemical equations. However, this form is too complicated for estimation. Therefore, this form is simplified to obtain a form that is suitable for estimation. This form is referred to as the estimation form.

2.1 The Electrochemical Form. For the purposes of this work, a battery model is partitioned into two parts: the SOC model representing the SOC system and the SOH model representing the SOH subsystem. The SOC system governs the battery SOC dynamics and determines the battery voltage as its output. The SOH subsystem governs the health process, with its output being the side reaction current density.

2.1.1 Battery State of Charge Model. The SOC model in this paper is the DFN model [30] as depicted in Fig. 1. In the DFN model, the structure of the solid phase in each electrode is modeled with a series of spherical particles, leading to spatial discretization along the thickness of the anode–separator–cathode sandwich, which is defined as the x dimension. The r dimension represents the direction along the radius of each spherical particle. The SOC is measured by the Li-ion concentration in the solid particles. Notice that the DFN model contains not only the SOC dynamics but also the dynamics regarding the Li-ion concentration in the electrolyte phase and potential. However, for simplicity, this model is referred to as the SOC model in this paper to differentiate it from the SOH model. The electrochemical equations of the DFN model are briefly summarized here for completeness, and the interested reader is referred to Ref. [31] for a detailed description.

Diffusion of Li-ions inside each electrode particle is governed by Fick's law along the r dimension, while diffusion within the electrolyte is along the x dimension, i.e.,

$$\frac{\partial c_{s,j}}{\partial t} = \nabla_r (D_{s,j} \nabla_r c_{s,j}) \tag{1}$$

$$\frac{\partial c_e}{\partial t} = \frac{\partial}{\partial x}\left[D_{e,j} \frac{\partial c_e}{\partial x} + \frac{1 - t^+}{\varepsilon_{e,j} F} i_e \right] \tag{2}$$

with the boundary conditions

$$\frac{\partial c_{s,j}}{\partial r}(0_r, t) = 0 \tag{3}$$

$$\frac{\partial c_{s,j}}{\partial r}(R_j, t) = -\frac{J_{1,j}}{D_{s,j} F a_{s,j}} \tag{4}$$

$$\frac{\partial c_e}{\partial x}(0_j, t) = 0 \tag{5}$$

$$\varepsilon_{e,n} D_{e,n} \frac{\partial c_e}{\partial x}(L_n, t) = \varepsilon_{e,\text{sep}} D_{e,\text{sep}} \frac{\partial c_e}{\partial x}(0_{\text{sep}}, t) \tag{6}$$

$$\varepsilon_{e,\text{sep}} D_{e,\text{sep}} \frac{\partial c_e}{\partial x}(L_{\text{sep}}, t) = \varepsilon_{e,p} D_{e,p} \frac{\partial c_e}{\partial x}(L_p, t) \tag{7}$$

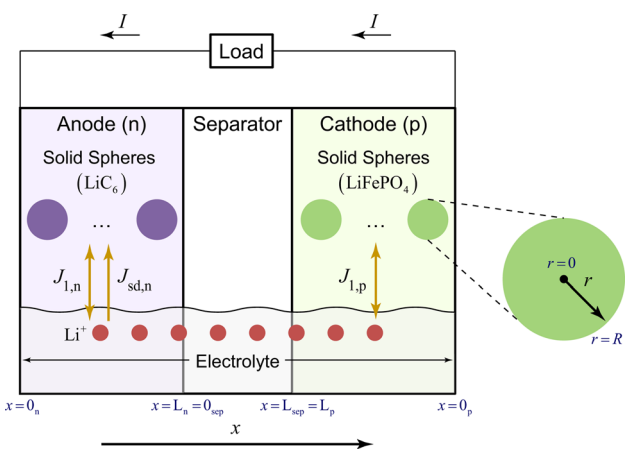

Fig. 1 The schematic of the electrochemical model of a $LiFePO_4$ battery

$$c_e(L_n,t) = c_e(0_{\text{sep}},t) \tag{8}$$

$$c_e(L_{\text{sep}},t) = c_e(L_p,t) \tag{9}$$

The SOC is computed from $c_{\text{s,n}}$ through

$$\theta_n = \frac{c_{s,n}}{c_{s,\max,j}} \tag{10}$$

which measures the percentage of the solid concentration with respect to the theoretical maximal Li-ion concentration. Then the SOC is computed as

$$\text{SOC} = \frac{\theta_n - \theta_{n,0\%}}{\theta_{n,100\%} - \theta_{n,0\%}} \times 100\% \tag{11}$$

where $\theta_{n,100\%}$ and $\theta_{n,0\%}$ are θ_n at the full-charge and depleted states, respectively [29].

The distributions of the potential in both the solid and electrolyte phases are along the x dimension

$$\frac{\partial \phi_{s,j}}{\partial x} = \frac{i_e - i_{\text{total}}}{\sigma_j^{\text{eff}}} \tag{12}$$

$$\frac{\partial \phi_e}{\partial x} = \frac{2RT}{F}(1-t^+)\left(1 + \frac{\mathrm{d}\ln f_j}{\mathrm{d}\ln c_e}\right)\frac{\partial \ln c_e}{\partial x} - \frac{i_e}{\kappa^{\text{eff}}} \tag{13}$$

with the boundary conditions

$$\frac{\partial \phi_{s,j}}{\partial x}(L_j) = 0 \tag{14}$$

$$\phi_e(0_n,t) = 0 \tag{15}$$

$$\phi_e(L_n,t) = \phi_e(0_{\text{sep}},t) \tag{16}$$

$$\phi_e(L_{\text{sep}},t) = \phi_e(L_p,t) \tag{17}$$

The total superficial current density i_{total} in Eq. (12) is obtained by averaging the current I over the total area of electrodes A

$$i_{\text{total}} = \frac{I}{A} \tag{18}$$

where positive I indicates discharge. The superficial current density i_e is governed by

$$\frac{\partial i_e}{\partial x} = J_{\text{total},j} \tag{19}$$

$$i_e(0_j,t) = 0 \tag{20}$$

where $J_{\text{total},j}$ represents the sum of the current densities of all electrochemical reactions in the battery, including the intercalation reaction that governs the SOC process and the side reactions that govern the SOH process. Notice that there is neither an intercalation reaction nor a side reaction in the separator, i.e., $J_{\text{total,sep}} = 0$, and thus $i_e(x,t) = i_{\text{total}}$ for all $x \in [0_{\text{sep}}, L_{\text{sep}}]$.

The exchange of Li-ions between the solid electrodes and electrolyte is referred to as the intercalation reaction (represented by the double-sided arrows in Fig. 1). The intercalation reaction is reversible, and thus the Li-ions used in this reaction can be recycled for future reactions. This reaction is governed by the Butler–Volmer equation

$$J_{1,j} = i_{0,j}a_{s,j}\left[\exp\left(\frac{\alpha_{a,j}F}{RT}\eta_j\right) - \exp\left(-\frac{\alpha_{c,j}F}{RT}\eta_j\right)\right] \tag{21}$$

where

$$i_{0,j}(x,t) = k_j(c_{s,j}(R_j,t))^{\alpha_{c,j}} [c_e(x,t)(c_{s,\max,j} - c_{s,j}(R_j,t))]^{\alpha_{a,j}} \tag{22}$$

$$\eta_p = \phi_{p,s} - \phi_{p,e} - U_{\text{ref},p} \tag{23}$$

$$\eta_n = \phi_{n,s} - \phi_{n,e} - U_{\text{ref},n} - \frac{J_{\text{total},n}}{a_{s,j}}R_{\text{film}} \tag{24}$$

The intercalation current density $J_{1,j}$ indicates the speed of the charge and discharge process. The SEI film, whose resistance is captured by R_{film} in Eq. (24), is assumed to accumulate only on the anode [23].

The SPM, a simplified version of the DFN model, is also used in this paper when we examine the robustness against modeling error. The SPM models each electrode with only one particle, thus eliminating the representation of the distribution of Li-ions along the x direction. Since uniform distribution of the electrolyte concentration is assumed, Eqs. (2) and (5)–(9) can be eliminated. Compared with the SPM, the DFN model can represent charge and discharge dynamics more accurately for high current rates. Details about the SPM used in this paper can be found in Refs. [26] and [29].

2.1.2 Battery State of Health Model. The Arora model [21] is used to model the SOH subsystem in this work due to its ability to capture all electrochemical-based degradation mechanisms that consume cyclable Li-ions. The health model in Refs. [14,15] adopted from Ref. [23] is an example of the Arora model used specifically for the SEI film formation mechanism. The form of the Arora model also provides insight on how to choose the form of the subsystem model in RCSI.

In the Arora model, each degradation mechanism is captured by the Butler–Volmer equation for the corresponding irreversible side reaction [21] (represented by the one-way arrow in Fig. 1). The irreversibility of the side reactions leads to the consumption of cyclable Li-ions, causing capacity fade of the battery. The rate of the side reaction is captured with the side reaction current density $J_{\text{sd},j}$. For $LiFePO_4$ batteries, degradation is assumed to happen only in the anode [23]. Hence, in the cathode

$$J_{\text{sd},p} = 0 \tag{25}$$

while in the anode

$$J_{\text{sd},n} = -i_{0,\text{sd}}a_{s,n}\exp\left(-\frac{\alpha_{c,n}F}{RT}\eta_{\text{sd}}\right) \tag{26}$$

where the overpotential η_{sd} can be obtained by

$$\eta_{\text{sd}} = \phi_{s,n} - \phi_{e,n} - U_{\text{ref,sd}} - \frac{J_{\text{total},n}}{F}R_{\text{film}} \tag{27}$$

where $J_{\text{total},j}$ is the total current density, whose distribution is determined only by I, as shown in Eqs. (18)–(20).

The SOC and SOH processes are related through the total current density $J_{\text{total},j}$, i.e.,

$$J_{\text{total},j} = J_{1,j} + J_{\text{sd},j} \tag{28}$$

Hence, the side reactions affect the SOC process by reducing the available current density for the intercalation.

2.2 The Estimation Form. The form of the battery model in Sec. 2.1 is simplified in this section to obtain a form that is suitable for estimation. Moreover, since degradation is assumed to occur only in the anode [23], the side reaction current density in the cathode is always zero. Hence, in the rest of the paper, we are

concerned only with the side reaction current density in the anode, $J_{\text{sd},n}$, and represent it with a shorter notation, J_{sd}.

The SOC model is simplified into the state space form with two inputs and two outputs. First, the partial differential equations (PDEs) contained in the SOC model are reduced to finite dimension as a group of ordinary differential equations (ODEs). Specifically, the PDE (1) governing diffusion in the solid phase is reduced to finite dimension through a third-order Padé approximation of the Laplace transformation of Eq. (1) [32], whereas the spatial dimension of the PDE (2) governing diffusion in the electrolyte phase is discretized with the central difference method. Therefore, the state equations of the SOC model are obtained by stacking the ODEs reduced from PDEs (2) and (1). Then, the inputs to the SOC model are reformulated to be the exogenous input I and output of the SOH model J_{sd}. In the electrochemical form of the SOC model, the inputs are $J_{1,j}$ and I. However, in the simplified form, by applying (28) combined with the fact that $J_{\text{total},j}$ can be calculated from the current I alone, $J_{1,j}$ is expressed as a function of J_{sd} and I. Finally, two outputs are calculated from the SOC model, namely, the exogenous output V and the input y_ϕ to the SOH model. The exogenous output V is the difference between the potential of the solid phases of the two electrodes, i.e.,

$$V(t) = \phi_{s,p}(0_p, t) - \phi_{s,n}(0_n, t) \tag{29}$$

The input y_ϕ to the SOH model is defined in Eq. (32).

The electrochemical equations of the SOH model can be simplified into a linear static equation with only one parameter and one input y_ϕ, which is computed in the SOC model. Substituting Eq. (27) into Eq. (26) yields

$$J_{\text{sd}} = K_{\text{SOH}} y_\phi \tag{30}$$

where

$$K_{\text{SOH}} \triangleq -i_{0,\text{sd}} a_{s,n} \exp\left(\frac{\alpha_{c,n} F}{RT} U_{\text{ref,sd}}\right) \tag{31}$$

$$y_\phi \triangleq \exp\left(-\frac{\alpha_{c,n} F}{RT}\left(\phi_{s,n} - \phi_{e,n} - \frac{J_{\text{total},n}}{a_{s,n}} R_{\text{film}}\right)\right) \tag{32}$$

Note that K_{SOH} is a function of the parameters of the battery model among which $i_{0,\text{sd}}$ and $U_{\text{ref,sd}}$ are associated with the SOH process.

One of the benefits of the linear static formulation of the SOH model is that under the presence of several side-reaction-based degradation mechanisms, the total side reaction current density can be easily obtained by summing all the side reaction current densities. Assume that a total of κ side reactions happen simultaneously. Then, each side reaction follows

$$J_{\text{sd},\iota} = K_{\text{SOH},\iota} y_\phi, \quad \iota = 1, \ldots, \kappa \tag{33}$$

where $J_{\text{sd},\iota}$ and $K_{\text{SOH},\iota}$ are the side reaction current density and the health parameter for the ιth side reaction, respectively. Because the input y_ϕ is computed in the SOC model, all side reactions share the same y_ϕ. Therefore, the total side reaction current density is

$$J_{\text{sd}} = \sum_{\iota=1}^{\kappa} J_{\text{sd},\iota} = \sum_{\iota=1}^{\kappa} K_{\text{SOH},\iota} y_\phi = K_{\text{SOH}} y_\phi \tag{34}$$

where $K_{\text{SOH}} = \sum_{\iota=1}^{\kappa} K_{\text{SOH},\iota}$. Therefore, Eq. (34) is the counterpart of Eq. (30) when several side reactions are present.

Above all, the SOH model has the form

$$\mathcal{J}_{\text{sd}}(k) = \mathcal{K}_{\text{SOH}} \mathcal{Y}_\phi(k) \tag{35}$$

where the vectors $\mathcal{J}_{\text{sd}}(k)$ and $\mathcal{Y}_\phi(k)$ are constructed by stacking J_{sd} and y_ϕ for every particle in the anode. Assuming the anode contains N particles, $\mathcal{J}_{\text{sd}}$ and $\mathcal{Y}_\phi$ are given by

$$\mathcal{J}_{\text{sd}} \triangleq \begin{bmatrix} J_{\text{sd}}^1 \\ \vdots \\ J_{\text{sd}}^N \end{bmatrix}, \quad \mathcal{Y}_\phi \triangleq \begin{bmatrix} y_\phi^1 \\ \vdots \\ y_\phi^N \end{bmatrix} \tag{36}$$

The gain $\mathcal{K}_{\text{SOH}}$ is the diagonal matrix

$$\mathcal{K}_{\text{SOH}} \triangleq \begin{bmatrix} K_{\text{SOH}}^1 & & \\ & \ddots & \\ & & K_{\text{SOH}}^N \end{bmatrix} \tag{37}$$

where the superscripts $1, \ldots, N$ in Eqs. (36) and (37) are the particle indices.

If $K_{\text{SOH}}^1 = \cdots = K_{\text{SOH}}^N \triangleq K_{\text{SOH}}^{\text{unif}}$, then $\mathcal{K}_{\text{SOH}}$ can be reduced to the scalar gain $K_{\text{SOH}}^{\text{unif}}$. In this case, there is no need to differentiate the degradation processes in different particles, and the SOH model can be simplified from Eq. (35) to

$$J_{\text{sd}}^{\text{ave}} = K_{\text{SOH}}^{\text{unif}} y_\phi^{\text{ave}} \tag{38}$$

where

$$J_{\text{sd}}^{\text{ave}} \triangleq \frac{1}{N}\sum_{m=1}^{N} J_{\text{sd}}^m, \quad y_\phi^{\text{ave}} \triangleq \frac{1}{N}\sum_{m=1}^{N} y_\phi^m \tag{39}$$

In Eq. (38), the average of the side reaction current densities among all particles is used instead of $\mathcal{J}_{\text{sd}}$ to represent the total degradation rate of the battery.

In summary, the simplified form can be depicted by the block diagram in Fig. 2(*a*). The signals in Fig. 2(*a*) are defined as follows: (i) the measurable input w and output y_0 of the overall model are the current I and the voltage V, respectively; (ii) the output of the SOH model u is the side reaction current density J_{sd}; and (iii) the input y to the SOH model is y_ϕ. The equations for the SOC model are then put into the discrete form for computation purpose, i.e.,

$$x(k+1) = f(x(k), u(k), w(k)) \tag{40}$$

$$y(k) = g(x(k), u(k), w(k)) \tag{41}$$

$$y_0(k) = g_0(x(k), u(k), w(k)) \tag{42}$$

where states $x(k) \in \mathbb{R}^n$ reflect the battery SOC, the electrolyte concentration, and the potential distribution in the solid and electrolyte phase. The function $f(\cdot)$ in Eq. (40) represents Eqs. (1), (2), (12), (13), and (19), while $g(\cdot)$ in Eq. (41) and $g_0(\cdot)$ in Eq. (42) are static relationships represented by Eqs. (32) and (29), respectively. The SOH model is a linear static equation in the form of either Eq. (35) or Eq. (38). Both Eqs. (35) and (38) can be written as

$$u = \theta^{\text{T}} \phi \tag{43}$$

where u, θ, and ϕ represent $\mathcal{J}_{\text{sd}}$, $\mathcal{K}_{\text{SOH}}$, and $\mathcal{Y}_\phi$ in Eq. (35), or $J_{\text{sd}}^{\text{ave}}$, $K_{\text{SOH}}^{\text{unif}}$, and y_ϕ^{ave} in Eq. (38). Notice that the SOC model and the SOH model interact with each other through the signals u and y.

Similarly, the SPM also follows the form of Eqs. (40)–(43) with the same definitions for all the signals. However, compared with the DFN model, the SPM has only four states (i.e., $x(k) \in \mathbb{R}^4$), while the DFN model with 50 particles per electrode has 725 states (i.e., $x(k) \in \mathbb{R}^{725}$). Finally, Eq. (42) in the SPM can be simplified as [26]

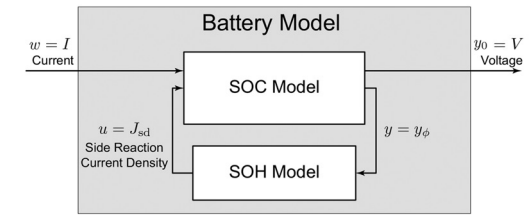

(*a*)

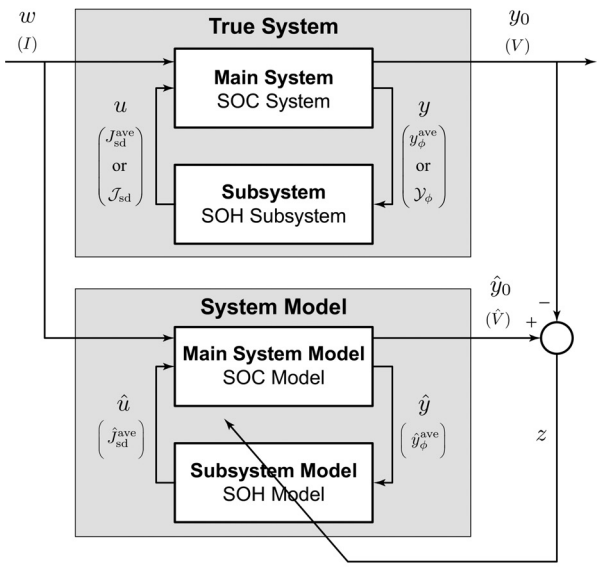

(*b*)

Fig. 2 The architectures of (*a*) the battery model and (*b*) retrospective-cost subsystem identification for estimation of the side reaction current density. Note that the output of the SOH model in (*a*) is the side reaction current density J_{sd}.

$$V = U_{\mathrm{ref},p} + \frac{RT}{\alpha F}\ln\left(\frac{i_{\mathrm{total}}}{2a_{s,p}L_p i_{0,p}} + \sqrt{\left(\frac{i_{\mathrm{total}}}{2a_{s,p}L_p i_{0,p}}\right)^2 + 1}\right) + \left(\phi_{s,n} - \phi_{e,n} - \frac{I}{AL_n a_{s,n}}R_{\mathrm{film}}\right) - \frac{1}{2A}\left(\frac{L_n}{\kappa^{\mathrm{eff},n}} + 2\frac{L_{\mathrm{sep}}}{\kappa^{\mathrm{eff,sep}}} + \frac{L_p}{\kappa^{\mathrm{eff},p}}\right)I - \frac{I}{AL_n a_{s,n}}R_{\mathrm{film}} \tag{44}$$

3 Retrospective-Cost Subsystem Identification

3.1 Problem Setup. Figure 2(*b*) presents the architecture of RCSI formulated for the proposed battery health estimation problem. The true system in the upper block contains a known main system and an unknown subsystem. The subsystem output, u, is the inaccessible signal to be estimated. This representation of the true system has the same architecture as the battery model in Fig. 2(*a*). The lower block, labeled "system model", is the model of the true system. The main system model is based on knowledge of the main system. The form of the subsystem model is assumed to be a mathematical approximation of the form of the true subsystem. The difference between the output of the true system and the system model is computed to identify the subsystem model parameter and thus estimate the subsystem output, the inaccessible signal of interest.

In the context of the battery health estimation problem, the true system is a battery, where the main system represents the battery SOC system, which is assumed to be known, and the unknown subsystem represents the battery SOH system to be identified. For the simulation study presented in this paper, the true system is represented by the battery model. The main system is the SOC model represented by Eqs. (40)–(42), while the subsystem is the SOH model represented by Eq. (43), where θ is assumed to be unknown.

Similarly, the system model is the battery model, where the main system model is the SOC model and the subsystem model is the SOH model. The SOC model in the main system model has the form

$$\hat{x}(k+1) = \hat{f}(\hat{x}(k), \hat{u}(k), w(k)) \tag{45}$$

$$\hat{y}(k) = \hat{g}(\hat{x}(k), \hat{u}(k), w(k)) \tag{46}$$

$$\hat{y}_0(k) = \hat{g}_0(\hat{x}(k), \hat{u}(k), w(k)) \tag{47}$$

If accurate knowledge of the main system is assumed, then the number of particles per electrode, which determines the number of states in Eqs. (40)–(42), and the parameters in the main system model are identical to those of the main system. In this case, $\hat{f}(\cdot)$ and $f(\cdot)$, $\hat{g}(\cdot)$ and $g(\cdot)$, and $\hat{g}_0(\cdot)$ and $g_0(\cdot)$ are identical. When modeling error between the main system model and the main system is considered, $\hat{f}(\cdot)$ and $f(\cdot)$, $\hat{g}(\cdot)$ and $g(\cdot)$, and $\hat{g}_0(\cdot)$ and $g_0(\cdot)$ are not identical.

For simplification in estimation, the SOH parameters for all of the particles in the subsystem model are assumed to be identical; thus, the form of the subsystem model is assumed to be a linear static equation as (38)

$$\hat{J}_{\mathrm{sd}}^{\mathrm{ave}} = \hat{K}_{\mathrm{SOH}}^{\mathrm{unif}}\hat{y}_\phi^{\mathrm{ave}} \tag{48}$$

where $\hat{J}_{\mathrm{sd}}^{\mathrm{ave}}$ and $\hat{y}_\phi^{\mathrm{ave}}$ are the estimates of the average of $\mathcal{J}_{\mathrm{sd}}$ and $\mathcal{Y}_\phi$, respectively; and $\hat{K}_{\mathrm{SOH}}^{\mathrm{unif}}$ is an estimate of the average of $\mathcal{K}_{\mathrm{SOH}}$ weighted by the subsystem input in each particle. When the SOH parameters are assumed identical for all of the particles in the true subsystem as well, that is, K_{SOH}^m are identical and Eq. (38) is used to represent the true SOH system, $\hat{J}_{\mathrm{sd}}^{\mathrm{ave}}$, $\hat{K}_{\mathrm{SOH}}^{\mathrm{unif}}$, and $\hat{y}_\phi^{\mathrm{ave}}$ are the estimates of $J_{\mathrm{sd}}^{\mathrm{ave}}$, $K_{\mathrm{SOH}}^{\mathrm{unif}}$, and y_ϕ^{ave}, respectively.

Define the output and input of the subsystem model as

$$\hat{u} \triangleq \hat{J}_{\mathrm{sd}}^{\mathrm{ave}} \tag{49}$$

$$\hat{y} \triangleq \hat{y}_\phi^{\mathrm{ave}} \tag{50}$$

Then, the subsystem model can be expressed in the ARMAX form

$$\hat{u}(k) = \hat{\theta}^{\mathrm{T}}(k)\hat{y}(k) \tag{51}$$

where $\hat{\theta}(k) \in \mathbb{R}^{l_u \times l_y}$ is the parameter of the subsystem model

$$\hat{\theta}(k) \triangleq \hat{K}_{\mathrm{SOH}}^{\mathrm{unif}}(k) \tag{52}$$

where l_u and l_y are the dimension of $\hat{u}$ and $\hat{y}$, respectively. In this paper, $\hat{\theta}$ and $\hat{\phi}$ are both scalars, and thus $l_u = 1$ and $l_y = 1$.

3.2 Algorithm Development. RCSI is developed under the assumption that both the main system and the subsystem are in discrete-time linear form. However, with a proper choice of parameters, the algorithm can also be applied to discrete-time nonlinear systems [14,15,33]. In this section, we present the development of RCSI in the linear context with guidelines to choose the parameters in nonlinear applications.

A two-stage Kalman filter version of RCSI is presented in this section, which is a variation of Refs. [14], [15], [33], and [34].

This version of RCSI operates recursively, where each time step contains two stages. In the first stage, the estimates of the inaccessible signal u in past time steps are constructed from the difference between the measurable signal y_0 and its estimate $\hat{y}_0$ using knowledge of the main system. These constructed estimates of u in the past time steps are referred to as retrospective-cost signals, and this stage is called retrospective-cost-based signal construction. Although the full model of the main system is assumed available, only the Markov parameters of this model are used in the signal construction, which simplifies the algorithm. In the second stage, the subsystem parameter is identified with the constructed estimates of u in past time steps using the Kalman filter. This identified subsystem parameter is then used in the subsystem model to generate $\hat{u}$ as a prediction of u in the next time step. These two stages are described next in detail.

3.2.1 Retrospective-Cost-Based Signal Construction. The main system is assumed to be linear and discrete-time with the form

$$x(k+1) = Ax(k) + Bu(k) + Fw(k) \tag{53}$$

$$y(k) = \mathrm{C}x(k) + Du(k) + Jw(k) \tag{54}$$

$$y_0(k) = E_1x(k) + E_2u(k) + E_3w(k)) \tag{55}$$

where $x(k) \in \mathbb{R}^n$ is the state, $w(k) \in \mathbb{R}^{l_w}$ is the external input, $u(k) \in \mathbb{R}^{l_u}$ is the output of the subsystem, $y(k) \in \mathbb{R}^{l_y}$ is the input to the subsystem, and $y_0(k) \in \mathbb{R}^{l_{y_0}}$ is the measurable output.

The main system is assumed known, and thus the model of the main system is constructed as

$$\hat{x}(k+1) = \hat{A}\hat{x}(k) + \hat{B}\hat{u}(k) + \hat{F}w(k) \tag{56}$$

$$\hat{y}(k) = \hat{C}\hat{x}(k) + \hat{D}\hat{u}(k) + \hat{J}w(k) \tag{57}$$

$$\hat{y}_0(k) = \hat{E}_1\hat{x}(k) + \hat{E}_2\hat{u}(k) + \hat{E}_3w(k) \tag{58}$$

$$z(k) = \hat{y}_0(k) - y_0(k) \tag{59}$$

where $\hat{x}(k) \in \mathbb{R}^n, \hat{y}(k) \in \mathbb{R}^{l_y}, z(k) \in \mathbb{R}^{l_z}, \hat{y}_0(k) \in \mathbb{R}^{l_{y_0}}, \hat{u}(k) \in \mathbb{R}^{l_u}$. The known information of the main system is reflected through matrices $\hat{A}, \ldots, \hat{E}_3$. If there is no modeling error in the main system model, then $\hat{A}, \ldots, \hat{E}_3$ are identical to $A, \ldots, E_3$, respectively. For nonlinear systems such as Eqs. (40)–(42), the linear equations (53), (54), and (55) are specializations of Eqs. (40), (41), and (42), respectively. Similarly, Eqs. (56), (57), and (58) are specializations of Eqs. (45), (46), and (47), respectively.

The main system model relates the subsystem model output $\hat{u}$ to the estimated output signal $\hat{y}_0$ using Markov parameters between $\hat{u}$ and $\hat{y}_0$, which are defined as

$$\hat{H}_i \triangleq \begin{cases} \hat{E}_2, & i = 0 \\ \hat{E}_1\hat{A}^{i-1}\hat{B}, & i \geq 1 \end{cases} \tag{60}$$

Markov parameters reflect the impact of the past input $\hat{u}$ on the current output $\hat{y}_0$ as in

$$\hat{y}_0(k) = \hat{E}_1\hat{A}^k\hat{x}(0) + \hat{E}_3w(k) + \sum_{i=0}^{k-1}\hat{E}_1\hat{A}^i\hat{F}w(k-i-1) + \sum_{i=0}^{k}H_i\hat{u}(k-i) \tag{61}$$

For nonlinear systems, the Markov parameters serve as tunable parameters in the algorithm, which also reflects the influence of $\hat{u}(k-i)$ on $\hat{y}_0(k)$. One way to tune $\hat{H}_i$ for nonlinear applications is to linearize the system around a point and use the linearization to determine $\hat{H}_i$.

A set of dominant Markov parameters is defined that corresponds to the set of $\hat{u}(k-i)$ that has the largest impact on the output $\hat{y}_0(k)$. The dominant Markov parameters and the corresponding $\hat{u}(k-i)$ can be put into the matrix form

$$\mathcal{H} \triangleq [H_{i_0} \quad \cdots \quad H_{i_r}] \in \mathbb{R}^{l_z \times rl_u} \tag{62}$$

$$U(k-1) \triangleq [\hat{u}^{\mathrm{T}}(k-i_0) \cdots \hat{u}^{\mathrm{T}}(k-i_r)]^{\mathrm{T}} \tag{63}$$

where r is a positive integer indicating the size of the set of dominant Markov parameters, and $i_0, \ldots, i_r$ are indices of the dominant Markov parameters.

Combining Eqs. (59) and (61)–(63) yields

$$z(k) = \mathcal{S}(k) + \mathcal{H}U(k-1) \tag{64}$$

where

$$\mathcal{S}(k) \triangleq \hat{E}_1\hat{A}^k\hat{x}(0) + \hat{E}_3w(k) + \sum_{i=0}^{k-1}\hat{E}_1\hat{A}^i\hat{F}w(k-i-1) - y_0(k) + \mathcal{H}'U'(k-1) \tag{65}$$

$\mathcal{H}'$ is the matrix containing all the Markov parameters H_i except the dominant ones and $U'(k-1)$ is the matrix containing $u(k-i)$ corresponding to the entries in $\mathcal{H}'$.

To utilize the information from several time steps, Eq. (64) can be rewritten with a delay of k_j time steps in the form

$$z(k-k_j) = \mathcal{S}_j(k-k_j) + \mathcal{H}_jU_j(k-k_j-1) \tag{66}$$

where $0 \leq j \leq s$ and $0 \leq k_1 < k_2 < \cdots < k_s$. Notice that the dominant Markov parameters can be different for different steps, i.e., $\mathcal{H}_j$ is not a constant with respect to j. The extended performance is defined by stacking $z(k-k_1), \ldots, z(k-k_s)$ into

$$Z(k) \triangleq [z^{\mathrm{T}}(k-k_1) \cdots z^{\mathrm{T}}(k-k_s)]^{\mathrm{T}} \in \mathbb{R}^{sl_z} \tag{67}$$

Therefore

$$Z(k) \triangleq \tilde{\mathcal{S}}(k) + \tilde{\mathcal{H}}\tilde{U}(k-1) \tag{68}$$

where

$$\tilde{\mathcal{S}}(k) \triangleq [\mathcal{S}(k-k_1) \cdots \mathcal{S}(k-k_s)]^{\mathrm{T}} \in \mathbb{R}^{sl_z} \tag{69}$$

$\tilde{\mathcal{H}} \in \mathbb{R}^{sl_z \times l\bar{U}}$ and $\tilde{U}(k-1) \in \mathbb{R}^{l\bar{U}}$. $\tilde{U}(k-1)$ is formed by stacking $U_1(k-k_1-1), \ldots, U_s(k-k_s-1)$ and removing repetitions in the components. $\tilde{\mathcal{H}}$ consists of the entries of $\mathcal{H}_1, \ldots, \mathcal{H}_s$ arranged according to the structure of $\tilde{U}(k-1)$.

The extended retrospective performance is defined by

$$Z^*(k) \triangleq Z(k) - \tilde{\mathcal{H}}\tilde{U}(k-1) + \tilde{\mathcal{H}}\tilde{U}^*(k-1) \tag{70}$$

where the actual past subsystem model outputs $\tilde{U}(k-1)$ in Eq. (68) are replaced by the retrospectively optimized subsystem outputs $\tilde{U}^*(k-1)$. Since the retrospective subsystem outputs serve as estimates of the true subsystem outputs in corresponding past steps, replacing $\tilde{U}(k-1)$ with $\tilde{U}^*(k-1)$ is expected to yield the smallest extended retrospective performance at the past steps. Therefore, the retrospective subsystem outputs can be found by minimizing the retrospective cost function defined as

$$\bar{J}(k) \triangleq Z^{*\mathrm{T}}(k)R_Z(k)Z^*(k) + \tilde{U}^{*\mathrm{T}}(k-1)R_U(k)\tilde{U}^*(k-1) \tag{71}$$

where $R_Z(k) \in \mathbb{R}^{l_z \times l_z}$ and $R_U(k) \in \mathbb{R}^{l_u \times l_u}$ are positive-definite weightings. In Eq. (71), $\tilde{U}^{*\mathrm{T}}(k)R_U(k)\tilde{U}^*(k)$ is the regularization term, which is included in $\bar{J}(k)$ to ensure that $\mathcal{A}(k)$ is invertible.

The unique global minimizer of Eq. (71) is

$$\tilde{U}^*(k-1) = -\frac{1}{2}\mathcal{A}^{-1}(k)\mathcal{B}(k) \tag{72}$$

where

$$\mathcal{A}(k) \triangleq \tilde{\mathcal{H}}^{\mathrm{T}} R_Z(k)\tilde{\mathcal{H}} + R_U(k) \tag{73}$$

$$\mathcal{B}(k) \triangleq 2\tilde{\mathcal{H}}^{\mathrm{T}} R_Z(k)[Z(k) - \tilde{\mathcal{H}}\tilde{U}(k-1)] \tag{74}$$

3.2.2 Kalman Filter Update of the Subsystem Parameter. Denote the component in $\tilde{U}^*(j-1)$ that estimates $u(k)$, where $k \le j$, with $\tilde{u}^*(k)$. By replacing $\hat{u}(k)$ in Eq. (35) with $\tilde{u}^*(k)$, identification of the subsystem becomes identification of the parameters in the ARMAX model

$$\tilde{u}^*(k) = \hat{\theta}^{\mathrm{T}}(k)\hat{y}(k) \tag{75}$$

where $\hat{\theta}(k)$ is defined in Eq. (52). If there are multiple choices of j such that $\tilde{U}^*(j-1)$ contains a component that estimates $u(k)$, then the selection of $\tilde{u}^*(k)$ is chosen to be the latest estimate.

The Kalman filter updating law for the ARMAX model parameters is

$$\begin{aligned}\hat{\theta}(k+1) = {} & [1-a(k)][\hat{\theta}(k) + (P(k+1)+Q)\hat{y}(k+1) \\ & \times [R_k + \hat{y}(k+1)^{\mathrm{T}}(P(k+1)+Q)\hat{y}(k+1)]^{-1} \\ & \times (u^*(k+1) - \hat{y}(k+1)\hat{\theta}(k))] + a(k)\hat{\theta}(0)\end{aligned} \tag{76}$$

The error covariance P is updated by

$$\begin{aligned}P(k+1) = {} & [1-a(k)][(P(k)+Q) - (P(k)+Q) \\ & \times (R_k + \hat{y}(k+1)(P(k)+Q)\hat{y}^{\mathrm{T}}(k+1))^{-1} + R_1] \\ & + a(k)P(0)\end{aligned} \tag{77}$$

where Q, R_k, and R_1 are the preset parameters. $a(k) \in \{0,1\}$ is an algorithm reset, that is, $\theta(k)$ and $P(k)$ are reset to their initial values when $a(k)=1$, otherwise $a(k)=0$. The error covariance matrix is initialized as $P(0) = \beta I$, where $\beta > 0$.

4 Simulation Results Under Ideal Conditions

This section presents simulation results of RCSI-based estimation of the side reaction current density under ideal conditions. The ideal conditions refer to the following conditions: (i) measurements of the input current and the output voltage contain no noise; (ii) exact knowledge of the battery SOC is assumed, and thus the initial SOC in the true system and the system model are set to be exactly the same; and (iii) no modeling error exists in both the main system model and the subsystem model.

The simulation results are obtained using two types of excitation signals. The first type is the constant current charge and discharge (CCCD) cycles. In every cycle, the battery model operates under the constant current charge (CCC) mode followed immediately by the constant current discharge (CCD) mode. The mode switches from CCD to CCC when the voltage reaches 2.0 V and from CCC to CCD at 3.6 V. Since the charge and discharge current for electric vehicles is below 10 C, 1 C and 10 C CCCD cycles are chosen to test the slow and fast charge/discharge cases, respectively [1]. For both cases, the SOC is initialized at 1%. Constant voltage modes are not included because the battery degradation is insignificant during constant voltage modes, which results in the unidentifiability of the SOH indicator [14,15].

The second type of excitation signals is the current profile generated from an electric vehicle following the Urban Dynamometer Driving Schedule (UDDS). This current profile evaluates the effectiveness of the algorithm under dynamic battery loading conditions typical for electric vehicle applications. In this paper, this UDDS current profile is generated by the Advisor software [35] with the default electric vehicle settings. The Li-ion battery in Advisor has a capacity of 7 Ah, while the rated capacity of the battery model in this paper is 2.5 Ah. Therefore, the current magnitude is scaled down to match the C rates and ensure that the battery is not overdischarged. The initial battery voltage is set to 3.6 V.

The parameters of the SOC model are adopted from Ref. [36], where the parameters are identified from the cycling data of commercial $LiFePO_4$ (Richmond, CA) batteries. The parameters of the SOH model are adopted from Ref. [23]. The number of particles in each electrode is obtained by increasing the number starting from ten at increments of ten until a further increment yields a voltage response difference less than 5 mV for the 10 C CCC mode. The number of particles is selected to be 50 per electrode. A sampling time of 0.2 s is chosen because the chemical reaction has slow dynamics. The results below also confirm that this sampling rate is fast enough to achieve accurate simulation and estimation.

For RCSI, the weights in the retrospective cost function (71) are set as $R_U = 0$ and $R_Z = 1$, and the parameters for Kalman filter update (76) and (77) are set as $Q = 0.1, R_k = 0.5$, and $R_1 = 0$. The parameter estimate and error covariance matrix are initialized at $\theta(0) = 0$ and $P(0) = 100$, respectively. The Markov parameter is set as $\tilde{\mathcal{H}} = H_0 = 2 \times 10^{-7}\ \Omega\,\mathrm{m}^3$.

The performance of RCSI is determined by the relative estimation errors of the side reaction current density and the subsystem parameter defined as

$$\varepsilon_{J_{\mathrm{sd}}} \triangleq \frac{J_{\mathrm{sd}} - \hat{J}_{\mathrm{sd}}}{J_{\mathrm{sd}}} \tag{78}$$

$$\varepsilon_{\theta} \triangleq \frac{\theta - \hat{\theta}}{\theta} \tag{79}$$

where J_{sd} and $\hat{J}_{\mathrm{sd}}$ are the true and estimated values of the side reaction current density, respectively; θ and $\hat{\theta}$ are the true and estimated values of the subsystem parameter, respectively.

To begin with, it is assumed that no discrepancy exists between the forms of the subsystem and subsystem model. Therefore, the SOH parameters K^m_{SOH} are set identical among all anode particles in the subsystem, and the form of the subsystem also follows Eq. (38). In this case, the variables to be estimated are $K^{\mathrm{unif}}_{\mathrm{SOH}}$ and $J^{\mathrm{ave}}_{\mathrm{sd}}$, whose estimates are $\hat{K}^{\mathrm{unif}}_{\mathrm{SOH}}$ and $\hat{J}^{\mathrm{ave}}_{\mathrm{sd}}$, respectively. Therefore, the variables in Eqs. (78) and (79) are named as follows:

$$J_{\mathrm{sd}} = J^{\mathrm{ave}}_{\mathrm{sd}}, \quad \hat{J}_{\mathrm{sd}} = \hat{J}^{\mathrm{ave}}_{\mathrm{sd}} \tag{80}$$

$$\theta = K^{\mathrm{unif}}_{\mathrm{SOH}}, \quad \hat{\theta} = \hat{K}^{\mathrm{unif}}_{\mathrm{SOH}} \tag{81}$$

$$y = y^{\mathrm{ave}}_{\phi}, \quad \hat{y} = \hat{y}^{\mathrm{ave}}_{\phi} \tag{82}$$

4.1 Constant Current Charge and Discharge Cycles. Figure 3(*a*) shows the estimates obtained with one 1 C CCCD cycle. The estimated parameter $\hat{\theta}$ converges to the true parameter θ in less than 1000 s after initialization at zero. Meanwhile, the estimated side reaction current density also converges to the true value. The relative estimation errors $\varepsilon_{J_{\mathrm{sd}}}$ and ε_{θ} are bounded within $\pm 2 \times 10^{-4}\%$ after the transient phase.

Figure 3(*b*) presents the estimates obtained with one 10 C CCCD cycle. The estimates of the subsystem parameter and the side reaction current density converge to their true values in less than 100 s. The relative estimation errors are bounded within $\pm 1\%$ after the transient phase.

The relative estimation errors show that the estimates diverge from their true values during the discharge mode. This divergence is due to the fact that the side reaction current density is near zero

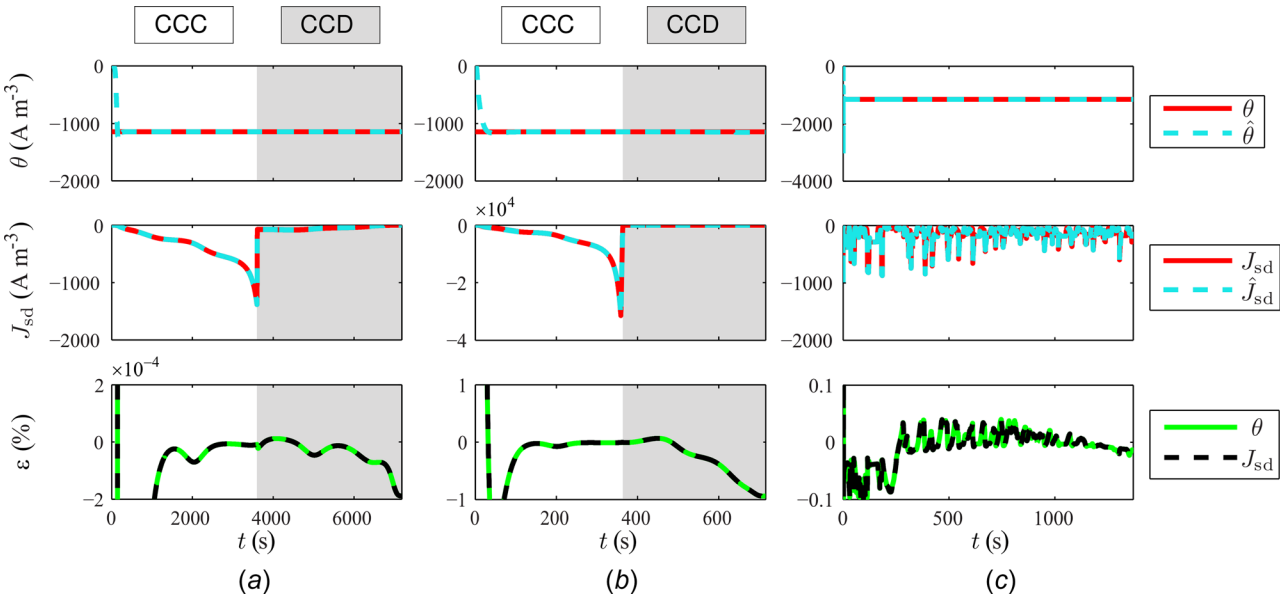

Fig. 3 The estimates and relative estimation errors ε of the subsystem parameter θ and the side reaction current density J_{sd} under ideal conditions with three input currents: (*a*) a 1 C CCCD cycle, (*b*) a 10 C CCCD cycle, and (*c*) a simulated current profile generated by an electric vehicle following an UDDS

during the discharge mode, which is consistent with the assumption in Ref. [23] that the degradation is negligible during discharge. As a result, the impact of the subsystem output on the output voltage is negligible; hence the identifiability of the subsystem parameter is weak. The divergence is more evident under the 10 C discharge rate, because the side reaction current density is smaller under the higher discharge C rate. During the 1 C discharge mode, the side reaction current density is on the order of 100 A/m^3, while it is on the order of 10 A/m^3 during the 10 C discharge mode. This divergence agrees with the conclusions in Refs. [14], [15], and [26].

It can be concluded from Figs. 3(*a*) and 3(*b*) that accurate estimates of the side reaction current density and health subsystem parameter can be obtained in both slow (1 C) and fast (10 C) constant current charge modes under ideal conditions. However, during the discharge modes, the estimates slowly diverge from their true values, due to the weak identifiability caused by the negligible side reaction current density.

4.2 The Urban Dynamometer Driving Schedule Test Cycles. Figure 3(*c*) shows the parameter estimates with the UDDS current profile. With $\hat{\theta}(0) = 0$, the parameter estimate $\hat{\theta}$ converges to the true parameter θ within 10 s. The estimate of the side reaction current density can also track the true value throughout the cycle. The relative estimation errors of both the side reaction current density and the subsystem parameter are bounded within $\pm 0.1\%$ after the transient phase. This result suggests that RCSI can estimate both the side reaction current density and the subsystem parameter effectively under the dynamic operating condition of electric vehicles under ideal conditions. The estimation errors show fluctuations when the true side reaction current density is small and the degradation is negligible, which agrees with the results in Sec. 4.1. The relative estimation errors also diverge at the end of the UDDS cycle. This divergence is due to the decrease of the battery SOC throughout the UDDS cycle except several brief moments of charging by regenerative braking. The SOC level drops to only 14% by the end of the cycle. The true side reaction current density is small when the battery SOC is low, which also leads to the weak identifiability.

In Fig. 3, the relative estimation errors in the side reaction current density and the health subsystem parameter are similar. On the one hand, x and $\hat{x}$ are close under ideal conditions. On the other hand, it can also be observed from Fig. 3 that convergence of the estimated side reaction current density is fast, so that $\hat{u}$ and u are close after the transient phase. Then, according to Eqs. (41) and (46), $\hat{y}$ and y are close when both x and $\hat{x}$, and u and $\hat{u}$ are close. Therefore

$$\varepsilon_{J_{sd}} = \frac{\theta y - \hat{\theta}\hat{y}}{\theta y} \approx \frac{\theta y - \hat{\theta} y}{\theta y} = \frac{\theta - \hat{\theta}}{\theta} = \varepsilon_\theta \tag{83}$$

Note that Eq. (83) holds as long as $\hat{y}(k) \approx y(k)$. Hence, Eq. (83) may be true, even without assuming the ideal conditions, when the differences between y and $\hat{y}$ caused by the discrepancies between x and $\hat{x}$, and J_{sd} and $\hat{J}_{sd}$ are small. However, if there is large measurement noise, or state or modeling errors that lead to a large difference between y and $\hat{y}$, the relative estimation errors in the side reaction current density and the health subsystem parameter may be different.

5 Robustness to Nonideal Conditions

In this section, robustness of the algorithm to nonideal conditions is examined. First, we show that the voltage difference between the true system and the system model caused by nonideal conditions (e.g., measurement noise, SOC estimation errors, main system modeling errors, and form discrepancy between the subsystem and the subsystem model) degrades the performance of the algorithm. Then, robustness against measurement noise, SOC estimation errors, and modeling errors are examined in Secs. 5.2, 5.3, and 5.4, respectively. Discussions of the simulation results are given next. Expectations about the performance of RCSI in practice based on the analysis of the simulation results are highlighted.

5.1 The Relationship Between the Estimation Accuracy and Voltage Errors. It can be observed from Eq. (71) that the goal of RCSI is to drive the optimal voltage difference, which corresponds to $Z^*(k)$ in Eq. (70), to zero, assuming that this zero voltage difference indicates that the optimal subsystem output $U^*(k-1)$ is identical to the true subsystem output. This assumption is not valid in the presence of a voltage difference caused by additional sources.

The impact of the side reaction current density on the output voltage is mainly through the intercalation reaction, and is manifested as an instantaneous impact. Because this instantaneous impact is small, the SOH estimation is sensitive to nonideal conditions that cause errors in the voltage. These nonideal conditions are the additional sources that cause an additional voltage difference, and this additional voltage difference is denoted by V_{as}.

Assuming Eq. (68) is corrected with V_{as}, it follows that

$$Z(k) = \tilde{\mathcal{S}}(k) + \tilde{\mathcal{H}}\tilde{U}(k-1) + V_{as} \tag{84}$$

Therefore, Eq. (70) is updated to

$$Z^*(k) = \tilde{\mathcal{S}}(k) + \tilde{\mathcal{H}}\tilde{U}^*(k-1) + V_{as} \tag{85}$$

According to the definition of dominant Markov parameters, $\tilde{\mathcal{H}}\tilde{U}(k-1)$ dominates $\tilde{\mathcal{S}}(k)$; thus, $\tilde{\mathcal{S}}(k)$ is considered negligible. Hence, Eq. (85) can be approximated as

$$Z^*(k) \approx \tilde{\mathcal{H}}\tilde{U}^*(k-1) + V_{as} \tag{86}$$

When the impact of V_{as} on $Z^*(k)$ is large, driving $Z^*(k)$ to zero induces an offset in $\tilde{U}^*(k-1)$ that compensates for the impact of V_{as}, which leads to an additional estimation error.

The additional relative estimation error α_{as} caused by V_{as} is given by

$$\alpha_{as} = V_{as}V_{J_{sd}}^{-1} \tag{87}$$

where

$$V_{J_{sd}} \triangleq \mathrm{Abs}(\tilde{\mathcal{H}}\tilde{U}^*(k-1)) \tag{88}$$

where $\mathrm{Abs}(\mathcal{A})$ denotes the matrix $\mathcal{A}$ with each entry replaced by its absolute value. Then the total relative estimation error is

$$\varepsilon_{total} = \varepsilon_{est} + \alpha_{as} \tag{89}$$

where ε_{est} is the relative estimation error under ideal conditions. Moreover, when α_{as} is required to be within a bound $\alpha_{as,bd}$, V_{as} needs to be within the bound

$$V_{as,bd} = \alpha_{as,bd}V_{J_{sd}} \tag{90}$$

In this paper, $Z^*(k)$, $\tilde{\mathcal{H}} = H_0$ and $\tilde{U}^*(k-1)$ are scalars. Then

$$V_{J_{sd}} = |H_0 J_{sd}(k)| \tag{91}$$

For the parameter values used in this paper, $H_0 = 2 \times 10^{-7}\ \Omega\,\mathrm{m}^3$; and for 1 C CCC mode, $|J_{sd}|$ is on the order of $10^3\,\mathrm{A\,m^{-3}}$ for most of the operating time. Therefore, $V_{J_{sd}} = |H_0 J_{sd}|$ is on the order of 10^{-4} V (0.1 mV) for most of the operating time. For this case, according to Eq. (90), if a bound of 10% for α_{as} is required, then $V_{as,bd}$ needs to be on the order of 0.01 mV. Similarly, when $V_{as,bd}$ is given, the corresponding $\alpha_{as,bd}$ can be computed from

$$\alpha_{as,bd} = V_{as,bd}/V_{J_{sd}} \tag{92}$$

In the rest of this section, the above analyses are verified by testing the robustness to measurement noise, SOC estimation errors, and modeling error, respectively. The 1 C CCCD cycle is used for excitation in this section except in the cases shown in Figs. 9(*b*) and 9(*c*) in Sec. 5.4.2. Based on the observation that the side reaction current density is less identifiable in the CCD mode, only the estimation results during the CCC mode are examined. Other excitations, such as 10 C CCCD cycles and UDDS cycles, can be analyzed in a similar manner.

The voltage differences between different battery models or different simulation situations are denoted as follows:

$$\delta V_{mod1/mod2} \triangleq V_{mod2} - V_{mod1} \tag{93}$$

$$\delta V_{sit1/sit2} \triangleq V_{sit2} - V_{sit1} \tag{94}$$

where the subscripts mod1 and mod2 denote two different models, while sit1 and sit2 denote two different simulation situations.

For simplicity, the names of different models are denoted as follows. The name DFNn denotes the DFN model with n particles per electrode. For example, the DFN model with 50 particles per electrode, which is the model used in Sec. 4, is denoted by DFN50. The name SPM denotes the single particle model.

5.2 Robustness to Measurement Noise. In this section, the input and output measurement noise levels are determined individually based on the desired relative estimation error bounds.

As an example, normal distributions with zero mean and tunable standard deviation are assumed for both the input and output measurement noise, i.e.,

$$I_{noise} \sim \mathcal{N}(0, \sigma_{In}^2)\ (\mathrm{mA}) \tag{95}$$

$$V_{noise} \sim \mathcal{N}(0, \sigma_{Vn}^2)\ (\mathrm{mV}) \tag{96}$$

σ_{In} and σ_{Vn} can be tuned based on the analysis in Sec. 5.1 and the desired relative estimation error bound. Here, a relative estimation error bound on the order of 10% is chosen as the desired estimation accuracy, and thus $|V_{as}|$ must be on the order of 0.01 mV.

Computing the effect of current measurement noise on voltage analytically is difficult because of the nonlinearity of the battery model. Hence, σ_{In} is selected numerically based on the simulated voltage response of DFN50 driven by a constant charge current that is 1 C with a perturbation ΔI. The battery model is simulated 11 times with ΔI set to 0 mA, ±100 mA, ±10 mA, ±1 mA, ±0.1 mA, and ±0.01 mA. The first simulation with $\Delta I = 0$ mA is the nominal case that records the voltage response of 1 C CCC mode without any perturbation in the input current. ΔV_i $(i = 2, \ldots, 11)$ is defined as the absolute voltage difference between the ith simulation and the first simulation, that is

$$\Delta V_i(k) \triangleq |V_i(k) - V_1(k)| \tag{97}$$

Figure 4 presents the box-and-whisker plots of ΔV_i corresponding to different ΔI. It can be observed that, in the cases that $\Delta I = \pm 1$ mA, $\Delta V_{6,7}(k)$ are generally on the order of 0.01 mV. Therefore, σ_{In} is chosen to be 1 mA.

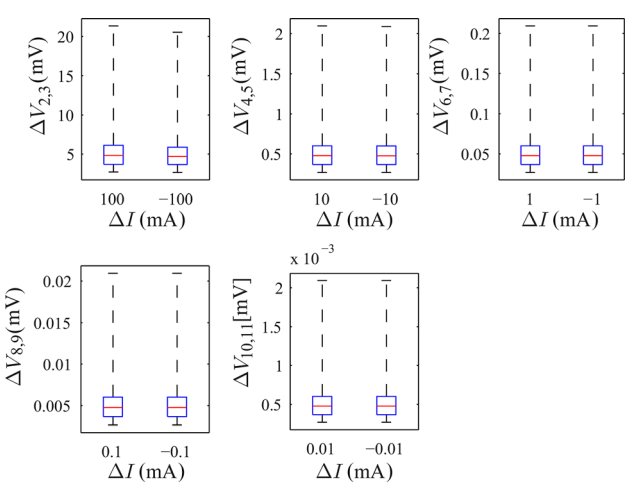

Fig. 4 The voltage difference ΔV of the DFN50 model caused by the current perturbation ΔI during the 1 C CCC mode

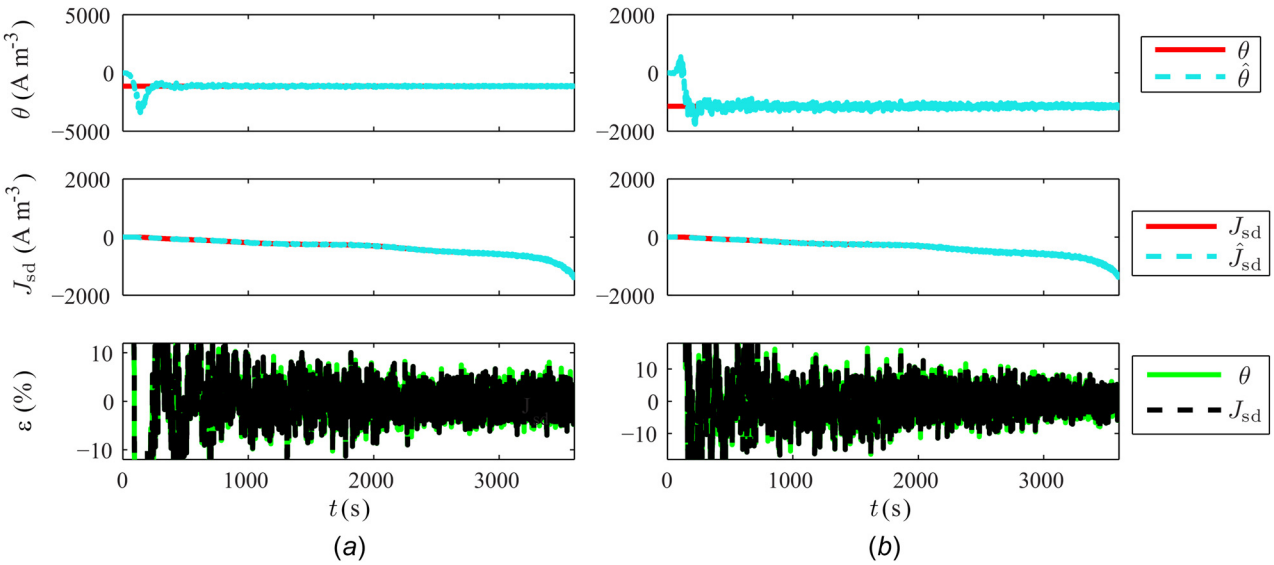

Fig. 5 The estimates and relative estimation errors ε of the subsystem parameter θ and the side reaction current density J_{sd} under the presence of (*a*) input and (*b*) output measurement noise. The bounds of the relative estimation errors are on the order of 10% as required.

Figure 5(*a*) shows the estimation results in the presence of input measurement noise with $\sigma_{In} = 1$ mA. The relative estimation errors are both bounded within $\pm 12\%$ after the initial transient phase, which is on the desired order of 10% for the relative estimation error bound.

The standard deviation of output measurement noise can be directly set to the level of required $|V_{as}|$, in this case 0.01 mV. Figure 5(*b*) presents the estimation results under output measurement noise with $\sigma_{Vn} = 0.01$ mV. The relative estimation errors are both bounded within $\pm 18\%$ after the initial transient phase, which is also on the desired order of 10%.

Therefore, assuming that the input and output measurement noise are zero mean, Gaussian, and white, the standard deviation for input and output measurement noise must be on the order of 1 mA and 0.01 mV, respectively, in the case where a relative estimation error bound on the order of 10% is required. For other relative estimation error bounds, the tolerable levels of measurement noise can be obtained in the same manner.

5.3 Robustness to State of Charge Estimation Errors. The estimation error in the SOC corresponds to the difference between the state of the main system and the state of the main system model. Because of the energy storage nature of batteries, the dynamics of solid concentration in each electrode contains a single integrator, hence the battery system is marginally stable with one eigenvalue at 1 for each electrode. Moreover, the states are not significantly affected by the subsystem, because the feedback from the side reaction current density on the main system dynamics is negligible. Therefore, the difference in the states that correspond to eigenvalues at 1 is persistent. The persistent state difference also causes a voltage difference between the true system and the system model, which causes error in the estimates of the side reaction current density and health subsystem parameter.

In this section, a 1% SOC estimation error is assumed because an error on this level is often expected in the SOC estimation [3,10,29]. The SOC in the true system is initialized at 1% as in Sec. 4, while the SOC in the system model is initialized at 2%. The estimation results are presented in Fig. 6(*a*). Both $\varepsilon_{J_{sd}}$ and ε_{θ} are on the order of 1000% for most of the operating time. Figure 6(*b*) presents the difference between the cases with 1% and 2% initial SOC levels in the voltage responses of DFN50 during the 1 C CCC mode. It can be observed that the voltage difference is on the order of 1 mV for most of the operating time. This level of

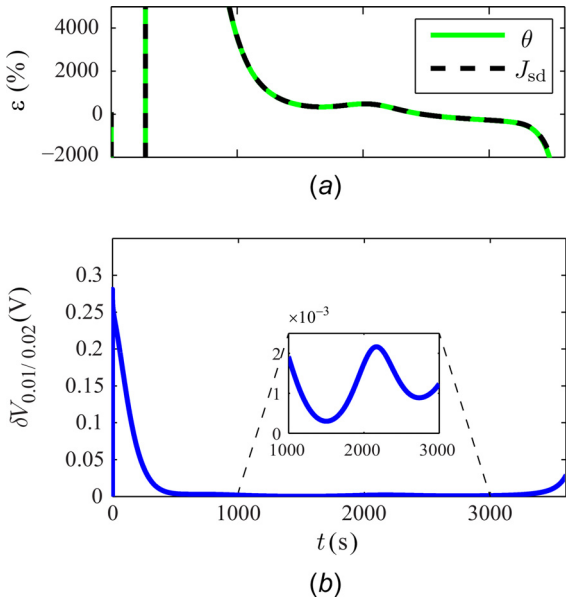

Fig. 6 (*a*) The relative estimation errors ε of the subsystem parameter θ and the side reaction current density J_{sd} and (*b*) the voltage difference under the presence of a 1% SOC error. The bound of the relative estimation errors in (*a*) is on the same order as expected from the voltage difference in (*b*).

voltage difference leads to a value of α_{as} on the order of 1000%, which agrees with the estimation results. The results indicate that the presence of an SOC estimation error can degrade the performance of RCSI in the estimation of side reaction current density. Therefore, an accurate estimation of the SOC is required to minimize the estimation error of the side reaction current density. Alternatively, co-estimation of the SOC and the side reaction current density can be pursued.

5.4 Robustness Against Modeling Error

5.4.1 Modeling Error in Main System Model. Many factors can contribute to the modeling error in the main system model, such as the truncation errors caused by approximating an infinite

dimensional system with a finite-dimensional system, parameter uncertainties, and discrepancies between the physical effects included in the mathematical model and the true physics.

5.4.1.1 Error in model structure. In this section, the impact of the main system modeling errors caused by the finite-dimensional approximation is analyzed as an example of the error in model structure. DFN50 is used as the true main system in the simulation, while either SPM or the DFN model with fewer particles per electrode (e.g., DFN30 and DFN10) is used as the main system model. The estimation errors caused by these modeling errors are compared with the anticipated estimation errors based on the voltage differences between different models to confirm the analysis in Sec. 5.1.

Figures 7(*a*)–7(*c*) present the relative estimation errors in cases with DFN30, DFN10, and SPM as the main system model, which are on the order of 100%, 1000%, and 10^4% for most of the operating time, respectively. Figures 7(*d*)–7(*f*) show the voltage difference under 1 C CCC mode between DFN50 and DFN30, DFN10, as well as SPM, which are on the order of 0.1 mV, 1 mV, and 10 mV for most of the operating time, respectively. Based on these voltage differences, according to Eq. (92), the anticipated estimation errors in the three cases are on the order of 100%, 1000%, and 10^4%, respectively. Therefore, the levels of anticipated estimation errors from the voltage differences in the three cases are all in accordance with the observed levels of the corresponding relative estimation errors.

Unlike all the other examples in this paper, Fig. 7(*c*) shows an appreciable discrepancy between $\varepsilon_{J_{sd}}$ and ε_θ. This is an example where a large modeling error in the main system model yields different relative estimation errors in the side reaction current density and health subsystem parameter by causing a large difference between y and $\hat{y}$. This result illustrates that the accuracy of the identified health subsystem parameter and of the estimated side reaction current density are not necessarily the same.

The results show that the modeling errors in the main system models degrade the accuracy of the estimated side reaction current density. The estimation is less accurate with a smaller number of particles per electrode in the main system model. Therefore, the estimation of the side reaction current density using RCSI requires a high fidelity battery model with very small voltage difference from the real battery.

A competing requirement for a high fidelity model is low computation complexity for real-time simulation and online estimation. For the DFN50 model used in this paper, the simulation is five times faster than the real-time on average. This time difference indicates that the computation required by the estimation algorithm designed in this paper can be done within a much shorter time than required for online estimation. The simulations in this paper are performed using MATLAB 2014 a on a 64-bit computer with 2.7 GHz processor. Although practical applications may not have this computational power, the computational speed gained by switching to a compiled language can partially offset the loss in the computational power. Methods also exist to significantly reduce the computational complexity of numerically solving the DFN model [32,37]. Therefore, even with the requirement of using a high fidelity model, the proposed method is still potentially suitable for online estimation.

5.4.1.2 Error in model parameters. In this section, we study the impact of parametric error caused by battery degradation on the estimation accuracy. Two parameters, R_{film} and $D_{s,n}$, are selected as the example parameters with error because they are reported to change as the $LiFePO_4$ battery degrades [16,18]. In particular, [18] reports 100% and 560% increase in R_{film} and diffusion coefficients D_s, respectively, after 600 hybrid pulse power characterization cycles at 25 °C. For the diffusion coefficients, only the one at the anode, namely, $D_{s,n}$, is increased because changes in the diffusion coefficient are caused by accumulation of the SEI film [18] and the SEI is herein assumed to grow only at the anode [23]. In this paper, we use the parameters for the fresh battery in the system model and increase R_{film} and $D_{s,n}$ in the true system according to the percentages reported in Ref. [18] to simulate the estimation of the side reaction current density in a degraded battery using the parameters for the fresh battery in the model.

Figures 8(*a*)–8(*c*) show the estimation results when the errors in R_{film} and $D_{s,n}$ are considered. It can be observed that the estimates $\hat{J}_{\text{sd}}$ and $\hat{\theta}$ stay close to their true values after 1000 s, and the relative estimation errors ε_θ and $\varepsilon_{J_{sd}}$ are both bounded within $[-15, 0]$%

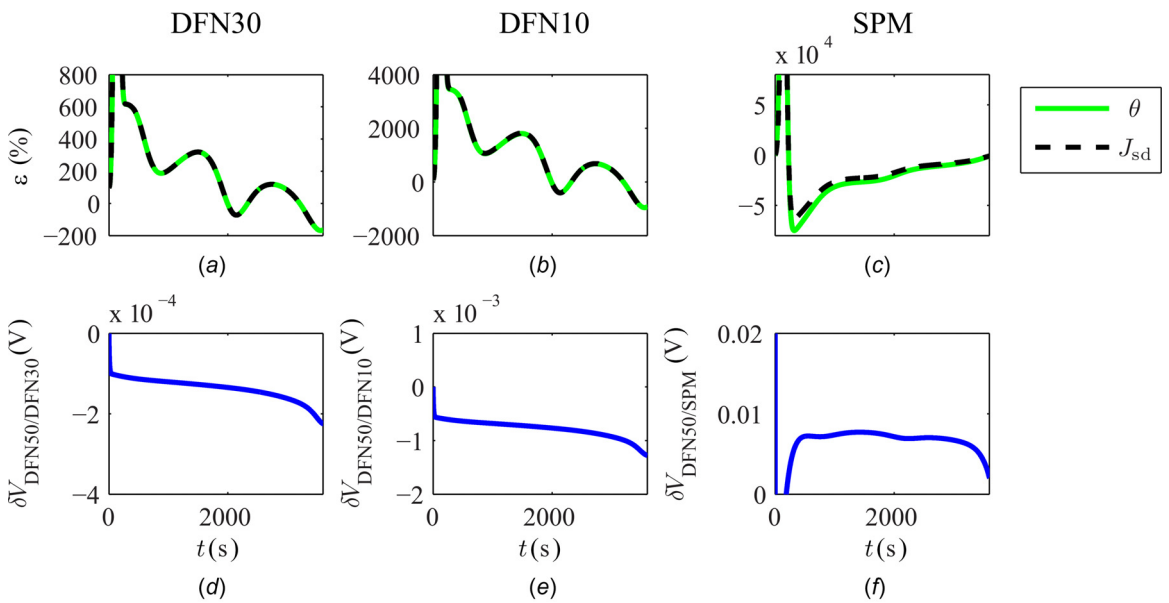

Fig. 7 The relative estimation errors ε of the subsystem parameter θ and the side reaction current density J_{sd} under the 1 C CCC mode with DFN50 as the true main system and (*a*) DFN30, (*b*) DFN10, and (*c*) SPM as the main system model. The differences in the voltage responses during 1 C CCC mode between DFN50 and (*d*) DFN30, (*e*) DFN10, and (*f*) SPM. The bounds of the relative estimation errors in (*a*), (*b*), and (*c*) are on the same orders as expected from the voltage differences in (*d*), (*e*), and (*f*), respectively.

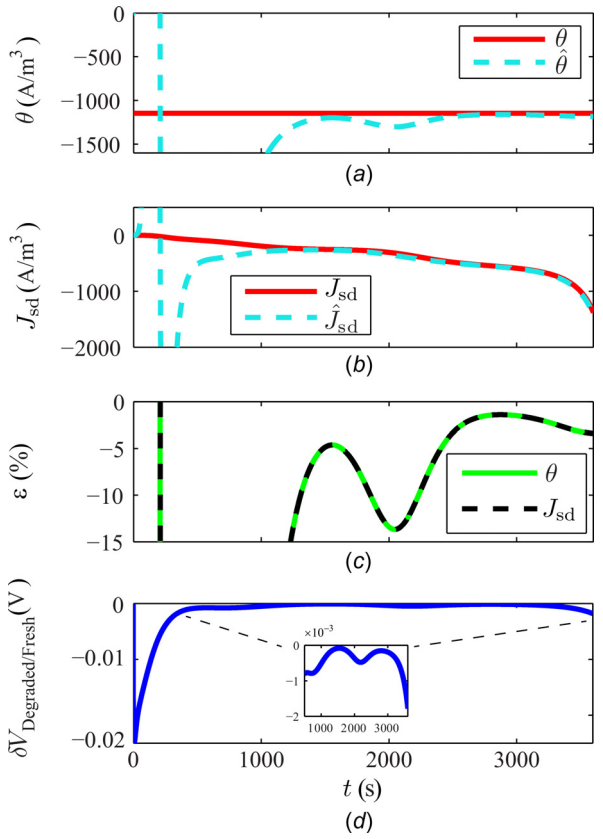

Fig. 8 The estimates of (*a*) the subsystem parameter θ and (*b*) the side reaction current density J_{sd}, and (*c*) relative estimation errors ε under parametric errors in R_{film} and $D_{s,n}$. (*d*) presents the voltage difference between the DFN50 model with values of R_{film} and $D_{s,n}$ in fresh and degraded batteries during 1 C CCC mode.

after 1200 s. Figure 8(*d*) shows the voltage difference, $\delta V_{\text{Degraded/Fresh}}$, between the DFN50 model with values of R_{film} and $D_{s,n}$ in fresh and degraded batteries during 1 C CCC mode. It can be observed that $\delta V_{\text{Degraded/Fresh}}$ starts on a level as high as 20 mV at the beginning of 1 C CCC mode, which corresponds to the region where the estimation errors are large. After 1200 s, when the relative estimation errors are on the order of 10% in Figs. 8(*a*)–8(*c*), $\delta V_{\text{Degraded/Fresh}}$ is on the order of 0.01–0.1 mV. Hence, the relative estimation error is on the same order as (when $\delta V_{\text{Degraded/Fresh}}$ is on the order of 0.01 mV) or one order of magnitude more accurate than (when $\delta V_{\text{Degraded/Fresh}}$ is on the order of 0.1 mV) what is expected from the analysis in Sec. 5.1. This is because J_{sd} and R_{film} are highly correlated, while the analysis in Sec. 5.1 assumes independence between J_{sd} and additional sources. Hence, $\delta V_{\text{Degraded/Fresh}}$ is a combined effect of the parametric errors and the change in J_{sd} caused by the parametric errors, which is larger than the voltage difference caused by the parametric errors alone. At the end of the 1 C CCC mode, although the voltage difference $\delta V_{\text{Degraded/Fresh}}$ increases to slightly over 1 mV, neither the magnitude nor the duration of this increase is significant enough to cause large changes in the estimates and thus the relative estimation errors stay below 10%. This result shows that the estimation of the side reaction current density is still accurate even under the considered parametric errors in $D_{s,n}$ and R_{film} introduced by battery aging.

5.4.2 Form Discrepancy Between Subsystem and Subsystem Model. It is hitherto assumed that the forms of the subsystem and the subsystem model are exactly the same. However, this assumption is usually not satisfied in practice. Moreover, representing a subsystem with a subsystem model of different form causes difficulty in subsystem identification, and results in less accurate estimates of the side reaction current density.

In this section, the performance of RCSI is examined when the form of the subsystem model is different from the form of the true subsystem. In particular, an example is provided to show how a subsystem model with identical SOH parameters can be used to estimate a true subsystem with nonidentical SOH parameters. Hence, the true subsystem follows the form as in Eq. (35), while the form of the subsystem model still follows (48). The following distribution of K^m_{SOH} is arbitrarily chosen for the true subsystem as an example:

$$k^m_{\text{SOH}} \sim \mathcal{N}(k_0, 25k_0^2) \tag{98}$$

$$K^m_{\text{SOH}} = |k^m_{\text{SOH}}| \tag{99}$$

where k_0 equals to the value of $K^{\text{unif}}_{\text{SOH}}$ in Sec. 4. Simulations show that distributions with higher covariances can lead to larger estimation error.

Furthermore, after removing the assumption in Eqs. (80)–(82) that no form discrepancy exists between the subsystem and the subsystem model, the following variables are re-defined in this section:

$$J_{\text{sd}} \triangleq \frac{1}{N}\sum_{m=1}^{N} J^m_{\text{sd}}, \quad \hat{J}_{\text{sd}} \triangleq \hat{J}^{\text{ave}}_{\text{sd}} \tag{100}$$

$$\theta \triangleq \frac{\sum_{m=1}^{N} K^m_{\text{SOH}} y^m_\phi}{\sum_{m=1}^{N} y^m_\phi}, \quad \hat{\theta} \triangleq \hat{K}^{\text{unif}}_{\text{SOH}} \tag{101}$$

$$y \triangleq \frac{1}{N}\sum_{m=1}^{N} y^m_\phi, \quad \hat{y} \triangleq \hat{y}^{\text{ave}}_\phi \tag{102}$$

Figure 9(*a*) presents the estimation results with 1 C CCC mode. Both $\varepsilon_{J_{\text{sd}}}$ and ε_θ are within $\pm 20\%$ after the transient phase. Simulations show that the voltage difference is generally on the order of 10^{-3} V between DFN50 with the health subsystem parameters following the distribution in Eqs. (98) and (99) and DFN50 with the health parameters all equal to the weighted average of the true parameters. This indicates that the relative estimation errors are expected to be on the order of 10%, which agrees with the $\pm 20\%$ bound in the estimates.

Besides the 1 C CCC mode, the UDDS cycle is also used as the excitation to examine the impact of form discrepancy in the subsystem model. Figure 9(*b*) presents the estimation results with the UDDS cycle, where the relative estimation errors are both within $\pm 20\%$ during the whole cycle. Oscillations during the whole cycle and divergence at the end of the cycle are present due to the weak identifiability caused by high discharge C-rate and low SOC level as in Fig. 3(*c*).

The estimation errors can be reduced by shutting down the estimation algorithm during high C-rate discharge when the true side reaction current density is small. In this case, the algorithm operates only when the input current can produce a large true side reaction current density, which is also the time when an estimate of the side reaction current density is needed. The threshold of the discharge C-rate for which the algorithm is shut down is chosen based on the particular current profile to balance the number of effective data points for estimation and the identifiability. Figure 9(*c*) presents the estimation results of the same case as in Fig. 9(*b*), but with the algorithm shut down whenever the discharge current is above 5 C. Comparison between Figs. 9(*b*) and 9(*c*) shows an improvement in the bound for the relative estimation errors from $\pm 20\%$ to $[-15, 10]\%$. This improvement in the estimation accuracy can be more significant when the excitation current is more aggressive.

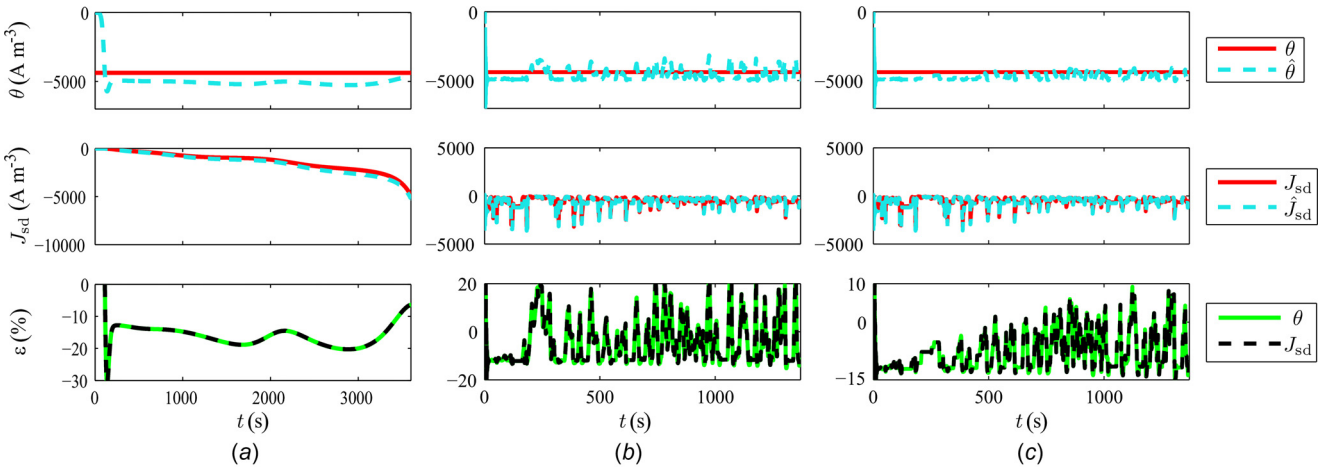

Fig. 9 The relative estimation errors ε of the subsystem parameter θ and the side reaction current density J_{sd} under (*a*) the 1 C CCC mode and (*b*) the UDDS cycle under the presence of form discrepancy between the subsystem and the subsystem model. (*c*) presents the relative estimation errors under the same UDDS cycle as in (*b*), but with the estimation algorithm shut down whenever discharge current is above 5 C. Note that shutting down the estimation algorithm during high C-rate discharge reduces estimation errors.

Similarly, to address the identifiability issue associated with low SOC, limiting the SOC region during which the estimation algorithm is operated can further improve the estimation accuracy near the end of the UDDS cycle. Because a low-accuracy SOC estimate suffices to determine the time to shut down the estimation algorithm, a possible method to estimate the true SOC level is Coulomb counting.

5.5 Discussions and Extensions of the Simulation Results. For all the results in this section, similar results can be obtained for other types of excitation current. The numerical results depend on $V_{J_{sd}}$ for the particular excitation type and the voltage errors caused by additional sources. Notice that even if one excitation type has a higher $V_{J_{sd}}$, it does not necessarily yield more robust estimation results, because the voltage difference caused by additional sources also varies among different excitation types. For example, in 10 C CCC mode, $V_{J_{sd}}$ is generally ten times higher than that for 1 C CCC mode. However, the expected bound for the relative estimation error in the 10 C case is not 1/10 of the bound for the 1 C case when there is modeling error in the main system model, because the voltage differences among the SPM and the DFN models are also larger for high C-rate. Therefore, the expected bound for the relative estimation error for one excitation type cannot be extrapolated to other excitation types. The robustness level for an excitation type can be obtained by following the framework developed in Sec. 5.1.

Furthermore, the expected performance of RCSI on real-life battery cycling data can be deduced by analyzing the difference between voltage responses of battery models and real-life battery measurement data. The result in Ref. [36], which identifies the parameter set used in this paper from experimental data, shows that the absolute error between the voltage measurements and the simulated voltage of the DFN model with this parameter set is below 40 mV for 80% of the time. This voltage error is about 10^3 larger than $V_{as,bd}$ identified in Sec. 5.1 that corresponds to the relative estimation error bound of 10%. This analysis indicates that estimation of the side reaction current density for the same battery under the same experimental condition in Ref. [36] is expected to be difficult given that the modeling error is relatively large compared to the voltage difference caused by the side reaction.

However, this does not mean that the side reaction current density cannot be estimated in practice. The results from the numerical analyses in Sec. 5 is applicable only to this particular battery parameter set, with this particular cycling profile, under this particular experimental condition. The side reaction current density can still be estimated successfully in other cases with different battery parameter sets, cycling profiles, or experimental conditions as long as they can make the corresponding V_{as} below the desired $V_{as,bd}$. Meanwhile, according to Eq. (90), given a desired $\alpha_{as,bd}$, $V_{as,bd}$ is a function of $V_{J_{sd}}$. Therefore, the side reaction current density can be successfully estimated within a reasonable $\alpha_{as,bd}$ even under the presence of practical nonideal conditions for scenarios where the battery parameters or the cycling profile yield a large $V_{J_{sd}}$.

The main generalizable conclusion that can be drawn from Sec. 5 is that the side reaction current density can be very sensitive to nonideal conditions that cause errors in the measurement or estimation of the voltage, because the side reaction current density is a small value that has a limited impact on the voltage. When this algorithm is applied to battery experiment data for the estimation of side reaction current density, the analysis in Sec. 5.1 needs to be followed in order to predict the margin for robustness.

Various methods can be applied to improve the robustness in estimation of the side reaction current density. To improve the robustness under the presence of measurement noise and modeling errors, very accurate sensors and models with higher fidelity are needed to obtain a value of V_{as} that satisfies the required $V_{as,bd}$. To improve the estimation accuracy of the side reaction current density under the presence of SOC estimation errors, the two step filter (TSF), a new inaccessible subsystem estimation algorithm, is developed and applied to a linearized single particle model in Ref. [38]. The application of the TSF to a nonlinear battery model requires additional research.

6 Summary and Conclusions

In this paper, the effectiveness of RCSI in estimation of the side reaction current density is explored. The side reaction current density is estimated directly for the first time as the SOH indicator. The battery SOH process that produces the side reaction current density is formulated as an inaccessible subsystem in the battery. The estimate of the side reaction current density is obtained by identifying the inaccessible battery SOH subsystem using RCSI. Robustness of the side reaction current density estimation is examined under various nonideal conditions, such as measurement noise, SOC estimation errors, modeling errors in the main system model, and the form discrepancy between the subsystem and the subsystem model.

When the ideal condition (i.e., no measurement noise, no SOC estimation error, and no modeling error) is assumed, the results show that RCSI can accurately and quickly estimate the side

reaction current density when the degradation effect is significant. An accurate estimation can be made throughout slow (1 C) and fast (10 C) CCCD cycles, and the UDDS cycle, with relative estimation errors bounded within $\pm 0.1\%$, $\pm 1\%$, and $\pm 0.3\%$, respectively.

This paper also explores the robustness of estimation of the side reaction current density to measurement noise, SOC estimation errors, modeling errors in the main system model, and the form discrepancy between the subsystem and the subsystem model separately. With the parameter set used in this work, the threshold for the voltage error caused by nonideal conditions is identified to be $O(0.01)$ mV so that the bound of the relative estimation errors is on the order of 10% under 1 C CCC mode. Based on this small threshold value, the algorithm is expected to be sensitive to nonideal conditions, which is a result of the side reaction current density having a small impact on the battery output voltage. However, these numerical results are specific to the particular parameter set and the cycling profiles considered in this paper. For other scenarios where the combination of the battery parameters and the cycling profile yield a larger $V_{J_{sd}}$ or a smaller V_{as}, the side reaction current density can be estimated with a smaller $\alpha_{as,bd}$ even under the presence of nonideal conditions. This paper also provides a procedure to predict the robustness margin given the particular battery parameter set and the cycling profile. Based on the results obtained, high fidelity models and accurate sensors would be needed in practice.

A potential limitation regarding the results in this paper is that the simulations are performed under the isothermal condition. Changes in operating temperature affect the degradation process [4,24,39,40], and thus a changing temperature may result in a changing health subsystem parameter, θ, which can affect the accuracy of the estimation of the side reaction current density. However, given the very fast convergence shown in the results herein, it is expected that the challenge presented by this changing parameter to the estimation of the side reaction current density is limited. To test this hypothesis, a more complete study can be performed incorporating thermal dynamics and cooling conditions by applying similar methods to electrochemical-thermal models [41,42].

The proposed method for estimating the side reaction current density is generally applicable to various Li-ion battery types and chemistries to monitor degradation caused by side reactions that consume cyclable Li-ions. Although all the numerical results in this paper are obtained from simulations using a parameter set for a $LiFePO_4$ battery, the proposed estimation technique, including the method for estimating the side reaction current density using RCSI and the framework analyzing its robustness, can also be applied to other parameter sets and other battery chemistries to monitor the SOH change resulting from any electrochemical-based degradation mechanism that consumes cyclable Li-ions.

In summary, this paper makes four main contributions. First, the side reaction current density is estimated as a direct SOH indicator for the first time. Second, the electrochemical model of the SOH subsystem is formulated as one linear static equation with all parameters lumped into one. This formulation provides a simple representation of the complicated SOH process, which in turn simplifies the design of the identification algorithm and facilitates the accurate identification of the SOH subsystem. The linearity of the subsystem model also allows easy combinations of several degradation mechanisms. Third, the side reaction current density and the SOH subsystem parameter are estimated using RCSI. Finally, a framework is provided to analyze the robustness of estimating the side reaction current density to nonideal conditions. The analyses from the framework are confirmed with simulation results, based on which predictions are made on the robustness of estimating the side reaction current density in practice.

Acknowledgment

This work is supported by U.S.-China Clean Energy Research Center - Clean Vehicles Consortium (Grant No. DE-PI0000012). The code for the DFN model and RCSI is revised from work of Professor Scott Moura from University of California, Berkeley [43], and Mr. Gerardo Cruz from University of Michigan, respectively. Their generosity is gracefully acknowledged.

Nomenclature

A = total area of sections, m^2
$a_{s,j}$ = specific surface area of porous electrodes, m^{-3}
$c_{h,j}$ = Li-ion concentration, mol m^{-3}
$c_{s,\max,j}$ = maximum concentration in the solid phase, mol m^{-3}
$D_{h,j}$ = diffusion coefficient, m^2 s^{-1}
F = Faraday constant, 96,487 C mol^{-1}
f_j = activity coefficient
I = current, A
$i_{h/\text{total}}$ = phasic/total superficial current density, A m^{-2}
$i_{0,j/\text{sd}}$ = intercalation/side reaction exchange-current density, A m^{-2}
$J_{1/\text{sd}/\text{total},j}$ = intercalation/side reaction/total current density, A m^{-3}
k_j = reaction rate, A m^4 mol^{-2}
r = coordinate along the radius of particles, m
R = universal gas constant, 8.314 J mol^{-1}
R_j = radius of electrode particles, m
R_{film} = solid-electrolyte-interphase film resistance, Ω m^2
t = time, s
T = temperature, K
t^+ = transference number
$U_{\text{ref},j/\text{sd}}$ = equilibrium potential for intercalation/side reaction, V
V = voltage, V
x = coordinate along the thickness of the anode–separator–cathode sandwich, m
0_r = the coordinate at the center of particles along r direction, m
$0_j/L_j$ = the coordinate at the starting/ending point of an electrode along the x direction, m

Greek Symbols

$\alpha_{a/c,j}$ = anodic/cathodic transfer coefficients of electrochemical reaction
$\varepsilon_{h,j}$ = volume fraction
$\eta_{j/\text{sd}}$ = overpotential for intercalation/side reaction, V
θ_j = stoichiometry of the solid electrode
$\theta_{j,0\%}$ = stoichiometry corresponding to a depleted battery
$\theta_{j,100\%}$ = stoichiometry corresponding to a fully charged battery
$\kappa^{\text{eff}}/\sigma_j^{\text{eff}}$ = conductivity of electrolyte/solid phase, S m^{-1}
$\phi_{h,j}$ = potential, V

Subscripts

h = phase name, where s and e stand for solid phase and electrolyte phase, respectively
j = section name, where p, n, and sep stand for cathode, anode, and separator, respectively

References

[1] Plett, G. L., 2004, "Extended Kalman Filtering for Battery Management Systems of LiPB-Based HEV Battery Packs—Part 1: Background," J. Power Sources, **134**(2), pp. 252–261.
[2] Plett, G. L., 2004, "Extended Kalman Filtering for Battery Management Systems of LiPB-Based HEV Battery Packs—Part 2: Modeling and Identification," J. Power Sources, **134**(2), pp. 262–276.
[3] Plett, G. L., 2004, "Extended Kalman Filtering for Battery Management Systems of LiPB-Based HEV Battery Packs—Part 3: State and Parameter Estimation," J. Power Sources, **134**(2), pp. 277–292.
[4] Wang, J., Liu, P., Hicks-Garner, J., Sherman, E., Soukiazian, S., Verbrugge, M., Tataria, H., Musser, J., and Finamore, P., 2011, "Cycle-Life Model for Graphite-$LiFePO_4$ Cells," J. Power Sources, **196**(8), pp. 3942–3948.
[5] Samad, N. A., Kim, Y., Siegel, J. B., and Stefanopoulou, A. G., 2016, "Battery Capacity Fading Estimation Using a Force-Based Incremental Capacity Analysis," J. Electrochem. Soc., **163**(8), pp. A1584–A1594.

[6] Weng, C., Cui, Y., Sun, J., and Peng, H., 2013, "On-Board State of Health Monitoring of Lithium-Ion Batteries Using Incremental Capacity Analysis With Support Vector Regression," J. Power Sources, **235**, pp. 36–44.
[7] Safari, M., Morcrette, M., Teyssot, A., and Delacourt, C., 2010, "Life-Prediction Methods for Lithium-Ion Batteries Derived From a Fatigue Approach—I. Introduction: Capacity-Loss Prediction Based on Damage Accumulation," J. Electrochem. Soc., **157**(6), pp. A713–A720.
[8] Safari, M., Morcrette, M., Teyssot, A., and Delacourt, C., 2010, "Life Prediction Methods for Lithium-Ion Batteries Derived From a Fatigue Approach—II: Capacity-Loss Prediction of Batteries Subjected to Complex Current Profiles," J. Electrochem. Soc., **157**(7), pp. A892–A898.
[9] Remmlinger, J., Buchholz, M., Soczka-Guth, T., and Dietmayer, K., 2013, "On-Board State-of-Health Monitoring of Lithium-Ion Batteries Using Linear Parameter-Varying Models," J. Power Sources, **239**, pp. 689–695.
[10] Andre, D., Appel, C., Soczka-Guth, T., and Sauer, D. U., 2013, "Advanced Mathematical Methods of SOC and SOH Estimation for Lithium-Ion Batteries," J. Power Sources, **224**, pp. 20–27.
[11] A123 Systems, 2012, "Nanophosphate High Power Lithium Ion Cell ANR26650m1-B Datasheet," Livonia, MI.
[12] Moura, S. J., Krstic, M., and Chaturvedi, N. A., 2012, "Adaptive PDE Observer for Battery SOC/SOH Estimation," ASME Paper No. DSCC2012-MOVIC2012-8800.
[13] Zhou, X., Stein, J. L., and Ersal, T., 2016, "Battery State of Health Monitoring by Estimation of the Number of Cyclable Li-Ions," ASME Paper No. DSCC2016-9730.
[14] D'Amato, A. M., Forman, J. C., Ersal, T., Ali, A. A., Stein, J. L., Peng, H., and Bernstein, D. S., 2012, "Noninvasive Battery-Health Diagnostics Using Retrospective-Cost Identification of Inaccessible Subsystems," ASME Paper No. DSCC2012-MOVIC2012-8649.
[15] Zhou, X., Ersal, T., Stein, J. L., and Bernstein, D. S., 2013, "Battery Health Diagnostics Using Retrospective-Cost System Identification: Sensitivity to Noise and Initialization Errors," ASME Paper No. DSCC2013-3953.
[16] Dey, S., Ayalew, B., and Pisu, P., 2015, "Nonlinear Adaptive Observer for a Lithium-Ion Battery Cell Based on Coupled Electrochemical–Thermal Model," ASME J. Dyn. Syst. Meas. Control, **137**(11), p. 111005.
[17] Tanim, T. R., and Rahn, C. D., 2015, "Aging Formula for Lithium Ion Batteries With Solid Electrolyte Interphase Layer Growth," J. Power Sources, **294**, pp. 239–247.
[18] Prasad, G. K., and Rahn, C. D., 2013, "Model Based Identification of Aging Parameters in Lithium Ion Batteries," J. Power Sources, **232**, pp. 79–85.
[19] Hatzell, K. B., Sharma, A., and Fathy, H. K., 2012, "A Survey of Long-Term Health Modeling, Estimation, and Control of Lithium-Ion Batteries: Challenges and Opportunities," American Control Conference (ACC), Montreal, Canada, June 27–29, pp. 584–591.
[20] Perkins, R. D., Randall, A. V., Zhang, X., and Plett, G. L., 2012, "Controls Oriented Reduced Order Modeling of Lithium Deposition on Overcharge," J. Power Sources, **209**, pp. 318–325.
[21] Arora, P., White, R. E., and Doyle, M., 1998, "Capacity Fade Mechanisms and Side Reactions in Lithium-Ion Batteries," J. Electrochem. Soc., **145**(10), pp. 3647–3667.
[22] Liu, P., Wang, J., Hicks-Garner, J., Sherman, E., Soukiazian, S., Verbrugge, M., Tataria, H., Musser, J., and Finamore, P., 2010, "Aging Mechanisms of $LiFePO_4$ Batteries Deduced by Electrochemical and Structural Analyses," J. Electrochem. Soc., **157**(4), pp. A499–A507.
[23] Ramadass, P., Haran, B., Gomadam, P. M., and White, R. E., 2004, "Development of First Principles Capacity Fade Model for Li-Ion Cells," J. Electrochem. Soc., **151**(2), pp. A196–A203.
[24] Safari, M., and Delacourt, C., 2011, "Aging of a Commercial Graphite/$LiFePO_4$ Cell," J. Electrochem. Soc., **158**(10), pp. A1123–A1135.
[25] Moura, S., Forman, J., Bashash, S., Stein, J., and Fathy, H., 2011, "Optimal Control of Film Growth in Lithium-Ion Battery Packs Via Relay Switches," IEEE Trans. Ind. Electron., **58**(8), pp. 3555–3566.
[26] Zhou, X., Ersal, T., Stein, J. L., and Bernstein, D. S., 2014, "Battery State of Health Monitoring by Side Reaction Current Density Estimation Via Retrospective-Cost Subsystem Identification," ASME Paper No. DSCC2014-6254.
[27] Santhanagopalan, S., Guo, Q., Ramadass, P., and White, R. E., 2006, "Review of Models for Predicting the Cycling Performance of Lithium Ion Batteries," J. Power Sources, **156**(2), pp. 620–628.
[28] Rahimian, S. K., Rayman, S., and White, R. E., 2013, "Extension of Physics-Based Single Particle Model for Higher Charge–Discharge Rates," J. Power Sources, **224**, pp. 180–194.
[29] Di Domenico, D., Stefanopoulou, A., and Fiengo, G., 2010, "Lithium-Ion Battery State of Charge and Critical Surface Charge Estimation Using an Electrochemical Model-Based Extended Kalman Filter," ASME J. Dyn. Syst. Meas. Control, **132**(6), p. 061302.
[30] Doyle, M., Fuller, T. F., and Newman, J., 1993, "Modeling of Galvanostatic Charge and Discharge of the Lithium/Polymer/Insertion Cell," J. Electrochem. Soc., **140**(6), pp. 1526–1533.
[31] Chaturvedi, N., Klein, R., Christensen, J., Ahmed, J., and Kojic, A., 2010, "Algorithms for Advanced Battery-Management Systems," IEEE Control Syst. Mag., **30**(3), pp. 49–68.
[32] Forman, J. C., Bashash, S., Stein, J. L., and Fathy, H. K., 2011, "Reduction of an Electrochemistry-Based Li-Ion Battery Model Via Quasi-Linearization and Padé Approximation," J. Electrochem. Soc., **158**(2), pp. A93–A101.
[33] D'Amato, A. M., Ridley, A. J., and Bernstein, D. S., 2011, "Retrospective-Cost-Based Adaptive Model Refinement for the Ionosphere and Thermosphere," Stat. Anal. Data Min., **4**(4), pp. 446–458.
[34] Morozov, A. V., Ali, A. A., D'Amato, A. M., Ridley, A. J., Kukreja, S. L., and Bernstein, D. S., 2011, "Retrospective-Cost-Based Model Refinement for System Emulation and Subsystem Identification," 50th IEEE Conference on Decision and Control and European Control Conference (CDC-ECC), Orlando, FL, Dec. 12–15, pp. 2142–2147.
[35] Brooker, A., Haraldsson, K., Hendricks, T., Johnson, V., Kelly, K., Kramer, B., Markel, T., O'Keefe, M., Sprik, S., Wipke, K., and Zolot, M., 2003, "Advanced Vehicle Simulator," National Renewable Energy Laboratory, Golden, CO, http://adv-vehicle-sim.sourceforge.net
[36] Forman, J. C., Moura, S. J., Stein, J. L., and Fathy, H. K., 2012, "Genetic Identification and Fisher Identifiability Analysis of the Doyle-Fuller-Newman Model From Experimental Cycling of a $LiFePO_4$ Cell," J. Power Sources, **210**, pp. 263–275.
[37] Cai, L., and White, R. E., 2009, "Reduction of Model Order Based on Proper Orthogonal Decomposition for Lithium-Ion Battery Simulations," J. Electrochem. Soc., **156**(3), pp. A154–A161.
[38] Zhou, X., Ersal, T., Stein, J. L., and Bernstein, D. S., 2015, "A Subsystem Identification Technique Towards Battery State of Health Monitoring Under State of Charge Estimation Errors," American Control Conference (ACC), Chicago, IL, July 1–3, pp. 1812–1817.
[39] Vetter, J., Novak, P., Wagner, M., Veit, C., Möller, K.-C., Besenhard, J., Winter, M., Wohlfahrt-Mehrens, M., Vogler, C., and Hammouche, A., 2005, "Ageing Mechanisms in Lithium-Ion Batteries," J. Power Sources, **147**(1), pp. 269–281.
[40] Tanim, T. R., Rahn, C. D., and Legnedahl, N., 2015, "Elevated Temperatures Can Extend the Life of Lithium Iron Phosphate Cells in Hybrid Electric Vehicles," ASME Paper No. DSCC2015-9763.
[41] Gu, W., and Wang, C., 2000, "Thermal-Electrochemical Modeling of Battery Systems," J. Electrochem. Soc., **147**(8), pp. 2910–2922.
[42] Guo, M., Sikha, G., and White, R. E., 2011, "Single-Particle Model for a Lithium-Ion Cell: Thermal Behavior," J. Electrochem. Soc., **158**(2), pp. A122–A132.
[43] Moura, S., 2014, "Doyle–Fuller–Newman Electrochemical Battery Model," GitHub, Inc., San Francisco, CA, https://github.com/scott-moura/dfn